Journal of the Korean Physical Society (2022) 80:817–851
https://doi.org/10.1007/s40042-022-00442-w

Online ISSN 1976-8524
Print ISSN 0374-4884

ORIGINAL PAPER - FLUIDS, PLASMA AND PHENOMENOLOGY

Plasma bioscience for medicine, agriculture and hygiene applications

Eun Ha Choi[1] · **Nagendra Kumar Kaushik**[1] · **Young June Hong**[1] · **Jun Sup Lim**[1] · **Jin Sung Choi**[1] · **Ihn Han**[1]

Received: 25 August 2021 / Accepted: 19 October 2021 / Published online: 4 March 2022

Abstract

Nonthermal biocompatible plasma (NBP) sources operating in atmospheric pressure environments and their characteristics can be used for plasma bioscience, medicine, and hygiene applications, especially for COVID-19 and citizen. This review surveyed the various NBP sources, including a plasma jet, micro-DBD (dielectric barrier discharge) and nanosecond discharged plasma. The electron temperatures and the plasma densities, which are produced using dielectric barrier discharged electrode systems, can be characterized as $0.7 \sim 1.8$ eV and $(3\text{–}5) \times 10^{14\text{–}15}$ cm^{-3}, respectively. Herein, we introduce a general schematic view of the plasma ultraviolet photolysis of water molecules for reactive oxygen and nitrogen species (RONS) generation inside biological cells or living tissues, which would be synergistically important with RONS diffusive propagation into cells or tissues. Of the RONS, the hydroxyl radical [OH] and hydrogen peroxide H_2O_2 species would mainly result in apoptotic cell death with other RONS in plasma bioscience and medicines. The diseased biological protein, cancer, and mutated cells could be treated by using a NBP or plasma activated water (PAW) resulting in their apoptosis for a new paradigm of plasma medicine.

Keywords Nonthermal biocompatible plasma (NBP) · Plasma bioscience and medicine · Hygiene applications · Virus inactivation · Cancer treatment · Plasma jet · Micro-DBD · Nanosecond discharged plasma · Plasma ultraviolet photolysis · Plasma activated water (PAW)

1 Introduction

A plasma is a group of electrically charged particles along with visible light, infrared, ultraviolet rays, neutral gases, excited reactive species, and some heat. It is the so-called fourth state of matters, the other three being the solid, liquid, and gaseous states. A plasma can be produced by using either a direct current (DC) or an alternating current (AC) electric discharge in a gas between powered and grounded electrodes [1–8]. The electric discharges produce electrons, ions, light, heat, and reactive neutral gases in high-energy excited states throughout the discharge processes. This matter is the basic substance for the creation of the universe, which is referred to in physics, as well as the source of life-forming substances in medical life science. The constituent gas of the plasma is negatively charged electrons, positively charged ions, neutral molecules in ground states and reactive oxygen and nitrogen species (RONS) with high chemical reactivity with their neighboring molecules [7–11].

The meaning of the plasma can be found more accurately by looking for a Sanskrit प्लाज़्मा (plasma) rather than a Greek (πλασμα) word. The Sanskrit word "Pla or pra" means very basic, primitive, very high, "z, s, or sura" means life or water, and "ma" means a collection of energy, i.e., matter [12]. Hence a plasma can be interpreted as a "fundamental and life substance or material in an universe with a highly accumulated state of energy". In medicine and biology, because "blood" and "proplasm" have been thought of as the primitive and essential material of life [13–15], they are called as "bio-plasma" and "plasma", respectively. Around 100 years ago, Irvine Langmuir named this kind of electrically discharged gas stream species as "plasma" after these properties which are similar to those of biological fluids.

In 1953, Stanley Miller performed discharge experiments under primitive atmospheric environments consisting of ammonia, methane, water vapor, and hydrogen gases and observed and watched the formation of amino acid such as alanine, glycine, and others [16]. These two or three amino

---

✉ Eun Ha Choi
ehchoi@kw.ac.kr

[1] Department of Electrical and Biological Physics, Plasma Bioscience Research Center and Applied Plasma Medicine Center, Kwangwoon University, Seoul 01897, Korea

acids are constituent molecules that can be combined to form a protein, which is the basic substance of life. Furthermore, life substances are known to be born through their polymerization. Meanwhile, an April 25, 1953, biologist Watson and physicist Crick reported that deoxyribose nucleic acid (DNA) is a genetic factor consisting of a double helix structure, which can give a deeper understanding of the molecular biology in fundamental life [17]. In modern medicine, all kinds of diseases, such as skin, dementia, cancers and dentals, occur due to the sudden mutation and oxidation of these cells. Proteins could have been generated by the synthesis of amino acids in the discharge state of the earth's primitive atmospheric environments. Based on these facts, we can treat the degenerate neural Alzheimer's and Parkinson's diseases, atopy, wounds and cancer. A hypothesis that plasma treatment is fundamentally possible may be established and realized for the next generation of plasma bioscience and medicine [5, 18–22]. Furthermore, it can be used in agriculture [23–34], oral health [35–43], and public health [44–49].

Low-temperature plasmas generated at ambient atmospheric pressure generally can be taken to have a cocktail form in which the RONS are mixed with electrons, ions, other neutrals and ultraviolet (UV) light. In particular, this type of nonthermal biocompatible plasma (NBP) is simply referred to as a nonthermal atmospheric pressure plasma (NAP) or a cold atmospheric pressure plasma (CAP) [5, 6, 11, 19, 50–65]. Here, we may call them simply as NBP. This kind of NBP has a slight thermal effect, as well as electrons and ions, reactive oxygen and nitrogen gases, ultraviolet and visible light. Figure 1a shows that the reactive neutral molecules with highly excited-energy in a NBP have strong reactivity with other molecules in prokaryotic and eukaryotic cells, as well as cell membrane and deoxyribose nucleic acid (DNA), by taking electrons from surrounding biomolecules or atom [66]. At this time, the atoms or molecules losing electrons are said to have been oxidized.

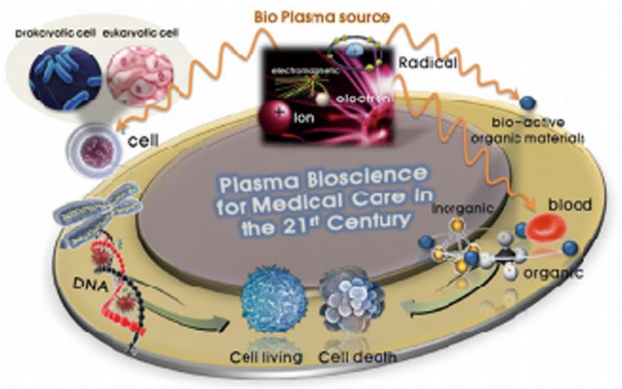

Fig. 1 Plasma bioscience and medicine with a nonthermal biocompatible plasma (NBP) [14]

Among the reactive species, the hydroxyl radical [OH], atomic oxygen [O], hydrogen peroxide [H_2O_2], singlet oxygen [$\uparrow O_2 \downarrow$], nitric oxide [NO], superoxide anion [$O_2{}^{*-}$], ozone [O_3], peroxynitrite [$ONOO^-$], nitrite [$NO_2{}^-$], nitrate [$NO_3{}^-$], and excited nitrogen molecules [$N_2{}^*$] play crucial roles in interactions with cells or microbials, as do their positive ions and electrons [5, 53, 54, 60]. Also, electromagnetic waves, such as ultraviolet, visible and infrared rays, are emitted from the excited gases of helium (He), argon (Ar), nitrogen (N_2), air, and their mixtures during the discharges in plasma. Interactions of these plasma generated RONS and electromagnetic waves with biological cells, tissues and microbials, such as bacteria, fungi, and viruses, can be used for wound treatment for tissue regeneration, selective cancer apoptosis, microbial biofilm removal, and public health, as shown in Fig. 1. Figure 1 shows selective ROS targeting cancer cells yielding to apoptosis, while normal cells experience proliferation, according to their exposed energy to plasma. The normal levels of ROS contents in normal and cancer cells are low and high, respectively [67]. If a plasma is used to treat both cells, then the ROS levels in those cells are increased; however, they are lower in normal cells and quite a bit higher than cytotoxicity threshold for inducing apoptosis in cancer cells, respectively [67]. Hence, the cancer cells selectively can be caused to undergo apoptosis due to a NBP.

Also, plasma medical devices, along with their safety standards, can be developed through research on biological interactions with plasma. Also, necessary data for plasma medical device development can be acquired through direct and indirect treatment of abnormal cell populations. Moreover, plasma treated water (PTW) [68–74], which is made by bombarding water with plasma, resulting in long-lived residual radicals and cells, can be used to interact with living tissues for many purposes.

The purpose of this review is to provide current studies and recent results of plasma bioscience and medicine based on plasma physics, chemistry, biology, and agriculture. Also, we review typical NBP sources, their plasma diagnostics, and their applications in cancer treatment, agriculture, and microbial treatment for bacteria removal and virus inactivation. Most NBP plasma sources are based on dielectric barrier discharged (DBD) plasmas, in which both or one of the electrodes is blocked by a dielectric material between them. There are two types of DBD plasmas: a pencil-type plasma jet and a surface discharged or facing discharged DBD plasma. These are frequently used with driving frequencies from less than 1 kHz up to microwave frequency ~ GHz. These NBP plasmas can be characterized by their electron densities from 10^{12} to ~ 10^{16} cm^{-3} and electron temperatures from ~ 0.8 to 3 eV [8, 14]. The plasma gas temperature in NBP plumes is very important for patients because heat at a temperature above 45 °C is not allowed by regulation.

2 Nonthermal biocompatible plasma (NBP) generator operating at atmospheric pressure

2.1 Nonthermal biocompatible plasma (NBP) generator

Many dielectric barrier discharge (DBD) plasma sources [57] for plasma medicines have been developed since E. W. von Siemens first studied them in 1857. These are known to be AC silent discharges with nonequilibrium atmospheric pressure plasma characteristics. DBD plasma sources can be manufactured using two types of geometrical configurations: a typical atmospheric-pressure nitrogen (or air) plasma jet based on DBD geometry as shown in Fig. 2a, and coplanar DBD (C-DBD) surface plasma types as shown in Fig. 2b. The plasma jet, which is currently very popular worldwide due to its ease of manufacture, and the C-DBD plasma whose electrode is based on a patent from plasma display panel technology [75, 76], can be used by the PBRC (Plasma Bioscience Research Center) to lead the development of health medicine, agriculture and fisheries, beauty, and environmental improvement for air, water and soil. The plasma jet system consists of a high voltage power supply and electrodes covered with dielectrics. A plasma jet device is assembled with a syringe and a glass or ceramic tube. A duty-cycled sinusoidal wave with a frequency of 60 Hz–1 GHz can be used in a plasma jet with a few kilovolts. A medical syringe or needle is used as a powered electrode and as guiding tube for the gas flow, and is made of stainless steel with an inner diameter is 1.2–3.3 mm and a thickness is 0.1–0.3 mm, which is tightly surrounded by a quartz tube whose outer diameter is 7–10 mm. The glass or quartz tube covering the needle also prevents electric shocks caused by high voltage across a bare needle and plays the role of a nozzle for the plasma plume. The outer grounded electrode is placed outside the end of the glass tube and is made of stainless steel with a central hole of 1 mm in diameter, through which the plasma is ejected into the surrounding ambient air. The discharge gap distance is adjusted to 2–3 mm between the inner and outer electrode. Air and any other gases or their mixtures can be used as the feeding gas. The electrical discharge can be produced and sustained by using two electrodes barriered by dielectric materials. These dielectrics are commonly made of glass, bakelite, quartz, ceramics, and polymers. Energetic electrons and ions are generated first on the dielectric surface discharge path, followed by volume discharges caused by ionization in the gases. Cells or biological targets have been treated with plasma jets for appropriate exposure times. The working temperature of the plasma source is in the range of 26–36 °C during plasma treatment [77].

Figure 2b shows a coplanar dielectric barrier discharged (C-DBD) plasma operating at ambient atmospheric pressure for biosciences, medicines and esthetics [77]. Biological tissue or skin have been treated by using C-DBDs for 30 s and a few minutes with operating voltages of 1–2.2 kV and discharge current 1–2 mA. The C-DBD plasma device consists of two parallel silver electrodes screen printed on a glass or ceramic substrate. The coplanar two electrodes whose thickness are about 3–5 um are separated by 100–200 um, and tightly screen printed by using SiO_2 paste with a thermal treatment at 600 °C. C-DBD plasma can be manufactured with diameter from 30 to 300 mm in diameter [77]. The discharge power is less than ~ 3 W. The working temperature of a plasma source is from 24 to 32 °C during plasma treatment. The distance between the two electrodes of a C-DBD can be changed from 0.1 mm to several centimeters. This can also be used for the generation of facing DBD discharged plasma by placing these two C-DBD panels opposite each

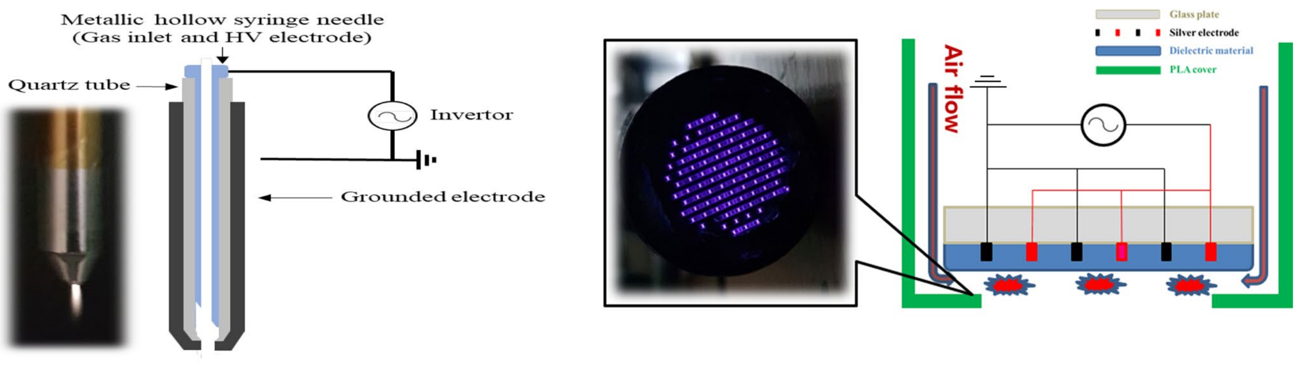

(a) (b)

Fig. 2 **a** Schematic of a typical atmospheric-pressure nitrogen (or air) plasma jet device with a 3 lpm nitrogen (or air) flow and the quartz dielectric tube; and **b** coplanar dielectric barrier discharged (C-DBD) surface plasma [77] other. Once gas is introduced through the peripheral guiding hole with a high voltage applied, the discharge is fired on the dielectric material, as shown in Fig. 2b.

The DBD-NBP can be applied for cancer cell death, skin care, wound and burn treatment, agricultural and marine products storage technology, semiconductor surface treatment and environmental improvement for air, water and soil. NBP devices operating at atmospheric pressure must regulate ozone, which should be less than 0.05 ppm in living environment [78, 79]; moreover, there must be no electric shock and no heat generated during plasma treatment of living tissue [5]. Especially a CDBD-NBP has made a remarkable contribution to pathogen sterilizer in ambulances. A CDBD-NBP approved as a very effective and efficient sterilization and disinfection device for use in ambulances, as well as many places, against COVID-19 throughout its inactivation test.

2.2 Basic discharge physics in dielectric barrier discharged (DBD) nonthermal biocompatible plasma (NBP) operating at ambient atmospheric pressure

Plasmas are rarely seen on the earth's surface. We, therefore, must make a plasma by using electrical breakdown. Figure 3 shows the schematic of discharge characteristics for coplanar DBD (C-DBD) type of nonthermal biocompatible plasma (NBP) with a gap distance d between the anode and cathode. Seed electrons in a space with an electric field E collide with neutrals, ionizing and generating new electrons. Here the ionization rate α is called as the first Townsend coefficient for ionization, which can be expressed in terms of electrical field E and the gas pressure P [75, 76, 80] as

$$\alpha\left(\frac{E}{P}\right) = AP\exp\left(-\frac{BP}{E}\right), \tag{1}$$

where A is a coefficient related to the ionization cross section, B represents an unique property of the gas characteristics such as the ionization potential energy, and P is the gas pressure between the anode and cathode separated by gap distance d. For neon gas, A and B are given by $A = 4$ and $B = 100$ [81]. The α represents the fraction of newly generated plasma electrons caused by ionizing electron collisions with neutral molecules as an electron travels by one millimeter along the electric field. The breakdown sustaining condition of a gas between the two electrodes with their gap distance d is given by $\gamma[M - 1] = 1$, where $M = e^{\alpha d}$ is the electron multiplication factor estimated at the anode and γ represents the secondary electron emission coefficient, called the Townsend second coefficient, due to low energy ions bombarding the cathode. The secondary electron emission coefficient γ, defined by $\gamma = I_e/I_i$, which is the emitted number of secondary electrons (I_e) from the cathode per ion colliding with the cathode (I_i). Normally, secondary electrons are generated by quantum mechanical Auger neutralization processes from the cathode surface when a low-energy ion whose energy is less than 100 eV approaches the cathode surface [82]. After some simple mathematics, the breakdown-sustaining condition can be rewritten as $\alpha(E/p)d = \ln(1 + 1/\gamma)$. If the ionization constant $\alpha(E/p)$ is substituted into the gas breakdown property, the breakdown voltage defined by $V_B = Ed$ can be expressed as [75, 76, 80, 81]

$$V_B(Pd) = \frac{BPd}{\ln\left[\frac{APd}{\ln\left(1+\frac{1}{\gamma}\right)}\right]}, \tag{2}$$

where the breakdown voltage V_B is a function of the Paschen parameter Pd, i.e., the product of the gas pressure P and the gap distance d between electrodes. The breakdown voltage for different discharge gases will be accordingly different from each other since their respective gas constant B and cathode property A are different to each other with different secondary electron emission coefficient γ, as shown in Eq. (2). Figure 4a shows the secondary electron emission coefficient γ versus incident neon ion energy on a cathode coated with a MgO layer with a crystalline orientation of

Fig. 3 Schematic of the discharge characteristics for a coplanar DBD (C-DBD) type of nonthermal biocompatible plasma (NBP) with a gap distance d between the anode and the cathode

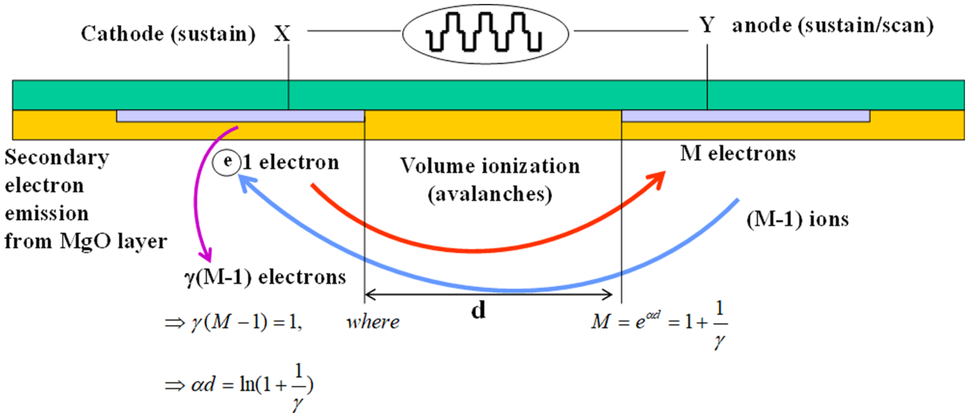

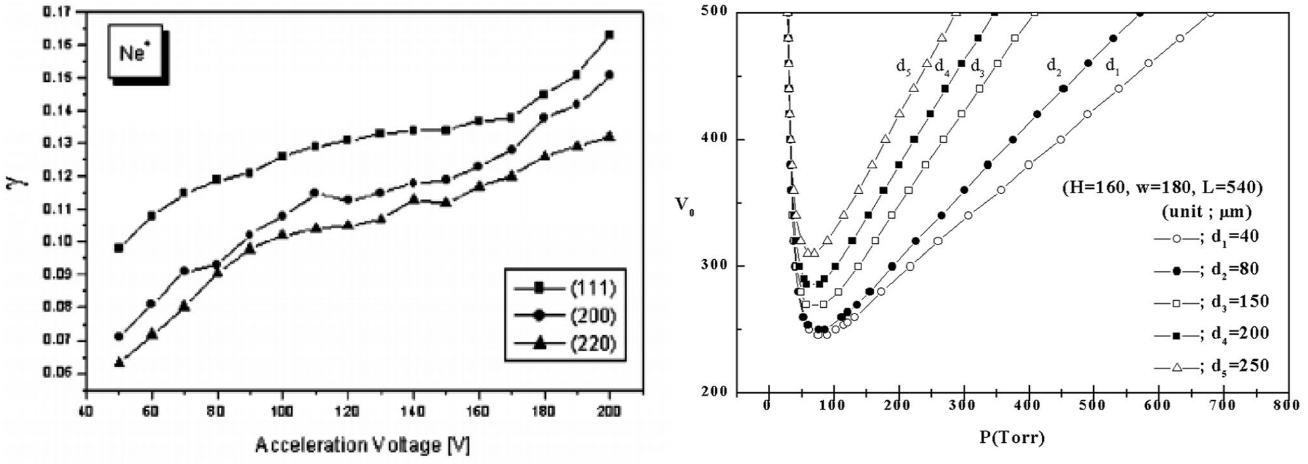

(a) (b)

Fig. 4 **a** Secondary electron emission coefficient γ for a MgO-coated cathode with respective crystalline orientations of (111), (200), and (220) versus incident neon ion energy in the range from 50 to 200 eV [83]; **b** breakdown voltage, i.e., Paschen curve, versus Paschen parameter Pd in units of Torr-cm for different gap distances from $d = 40$ μm to 250 μm calculated for the coplanar DBD geometry of Fig. 3 [81]

(111), (200), and (220). The neon ion energy is controlled to be in the range from 50 to 200 eV. For the (111) orientation of the MgO layer, the γ is about 0.1 at a neon energy of 50 eV [83]. Figure 4b shows a Paschen curve, the so-called breakdown voltage with a secondary electron emission coefficient $\gamma = 0.1$ in the calculations for different gap distances of 40, 80, 150, 200, and 250 um versus gas pressure P for a Ne discharge gas with anode or cathode width of $w = 180$ um and a $L = 540$ um for x-space limit of geometry in right hand side of Fig. 3 from its origin at a central point [81].

The minimum breakdown voltage V_M could be obtained from Eq. (2) by differentiating $V_b\,(Pd)$ with respect to Pd and setting the derivative to be zero, from which V_M is given by

$$V_M = 2.72\left(\frac{B}{A}\right)\ln\left(1+\frac{1}{\gamma}\right) \quad \text{at}(Pd)_{\min} = \left(\frac{2.72}{A}\right)\ln\left(1+\frac{1}{\gamma}\right) \tag{3}$$

where $(Pd)_{\min}$ is the value satisfying $\frac{dV_b}{d(Pd)} = 0$ for V_M. The breakdown voltage V_B increases when the value of Pd is too small, which is less than 1 Torr-cm. Also, according to the Eq. (3), each gas has its own minimum breakdown voltage V_M [75, 76, 80]. The discharge and its minimum voltage for the shorter gap distances are lower than those for longer one at gas pressure larger than 50 Torr.

3 Diagnostics of atmospheric pressure nonthermal biocompatible plasma (NBP)

3.1 Optical emission spectroscopy (OES) measurement

Optical emission spectroscopy (OES) can be performed to identify reactive species by using the emission characteristics of the nonthermal atmospheric pressure plasma. For this kind of work, the spectrometer must be calibrated for wavelength measurements by using an Hg–Ar lamp. The OES spectra could be obtained by using an optical fiber whose diameter is about 400 um placed in front of the nozzle of the plasma plume through which the emitted light is led to a slit for collection into a grating of the spectrometer.

The optical emission spectra (OES) of a soft plasma jet and a surface discharged micro-DBD are represented in Fig. 5a and b, respectively. Emission signals from the nitric oxide gamma band (NO-γ) at 236, 246, and 258 nm, and 283 nm whose energies are in the range of 3.27–5.25 eV [84] can be seen in both Fig. 5a and b. These are caused by the collisions of energetic electrons or metastable atoms with nitrogen molecules in air. Also, emission in the range of 306–309 nm, which are caused by hydroxyl radical (OH)

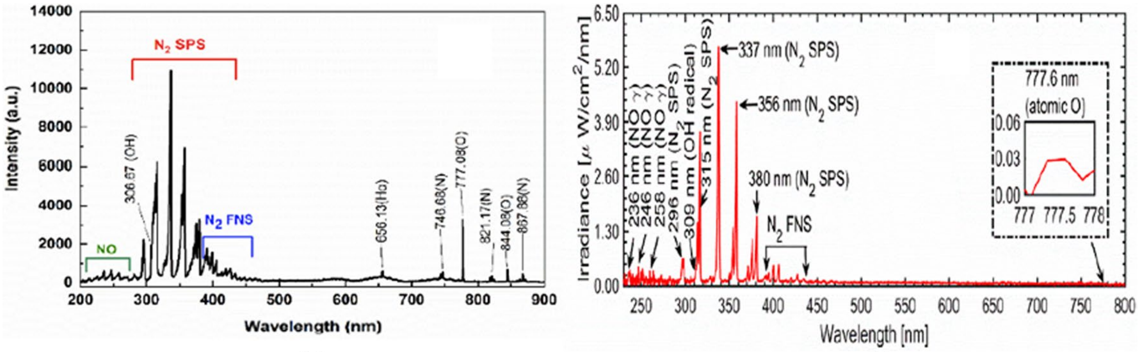

(a) (b)

Fig. 5 OES emission profiles from **a** the soft plasma jet and **b** the surface discharged micro-DBD plasma

species, which are produced by dissociating of water molecules, being present in the ambient environment [85]. The nitrogen second positive system (N2 SPS) is strongly observed at 296, 315, 337, 356, and 380 nm, etc.; moreover, the nitrogen first negative system (N2 FNS) emissions are weakly observed at wavelengths in the range of 390–440 nm [7, 86, 87]. These emissions, which originate from the excited nitrogen species, are caused by nitrogen molecules both in the feeding gas and the ambient environment. In addition to these, emissions from atomic oxygen (O) are seen at 777 nm and 844 nm, and the emission at 656 nm is from the hydrogen atom (H_α).

3.2 Measurement of the OH and the NO radical density using optical absorption spectroscopy

Reactive oxygen and nitrogen species (RONS) generated by a non-thermal atmospheric pressure plasma play an important role in many industrial fields. Radical generation from plasma sources is an important phenomenon for the development of plasma equipment because air plasmas can generate abundant RONS. The optical diagnostic technology of the plasma is very useful to control the amounts of chemical species. The ROS has a very short lifetime and is used to sterilize the biomaterials [5, 45]. The oxygen molecule is known to be critical for aerobic biological or physiological processes but it is converted to reactive oxygen species (ROS) about 5% of the time during the energy production processes [3]. These Reactive species are extremely toxic to cells and causing damage to other molecules and cell structures. The nitric oxide (NO), a type of reactive nitrogen species (RNS), performs an essential role in cell stimulus in human body organs [88]. Many researchers have measured these radicals by using optical absorption spectroscopy.

The hydroxyl radicals OH of ROS in a nonthermal atmospheric pressure plasma can be diagnosed by using the ultraviolet (UV) absorption spectroscopy. In Refs [86, 87 and 89], the experiment use of the ultraviolet absorption spectroscopy is shown. This system consists of a UV lamp, which is a Hg lamp whose power is 0.5 W centered at a wavelength of 306 nm and a plano-convex lens which transmits wavelength from ultraviolet to infrared [86]. The UV light passes through and is focused by a plano-convex lens with a diameter of 200 um in the plasma jet measurement, the absorption that occur at 309.2 nm, for the OH species [86]. The hydroxyl OH radical densities produced from air, argon, nitrogen, or any kind of gas plasma can be investigated by using Lambert–Beer's law. The intensity for the incident and the transmitted light passing through a plasma space whose thickness is x are denoted an I_o and I_v, respectively, and the density of the hydroxyl radical OH species produced by the plasma jet is given by [86, 87, 89, 90]

$$N = -\frac{1}{\sigma \cdot x} \ln\left(\frac{I_v}{I_0}\right) \tag{4}$$

where N is the density of hydroxyl OH radicals, and σ is the molecular cross-sectional area, which is about 6×10^{-7} cm^2 for OH species [86]; x is 0.3 cm. The hydroxyl radical OH density can be obtained from the experimental measurement of I_v / I_o, i.e., the ratio of the transmitted intensity to incident intensity, by using Eq. (4).

Figure 6a shows plots of the UV absorption profile, represented by the black line, caused by the OH radical species for a nonthermal Ar plasma jet whose gas flow rates range from 80 to 300 sccm versus wavelength [86]. Also, the reference UV lamp (I_o) and emission profiles from OH radical species in the nonthermal plasma without UV incidence are indicated by red and blue lines, respectively, in this figure. The strong OH absorption profiles appear at 309.2 nm, as shown in the dotted box, while no absorption is seen at ~ 307 nm. In this experiment, the absorbed signals appearing at ~ 317 nm have nothing to do with OH radicals. The absorbed UV profiles (black line) in Fig. 6a can be obtained by subtracting the emission profiles of OH radical (blue line) in plasma from the transmitted UV intensity (I_v) passing

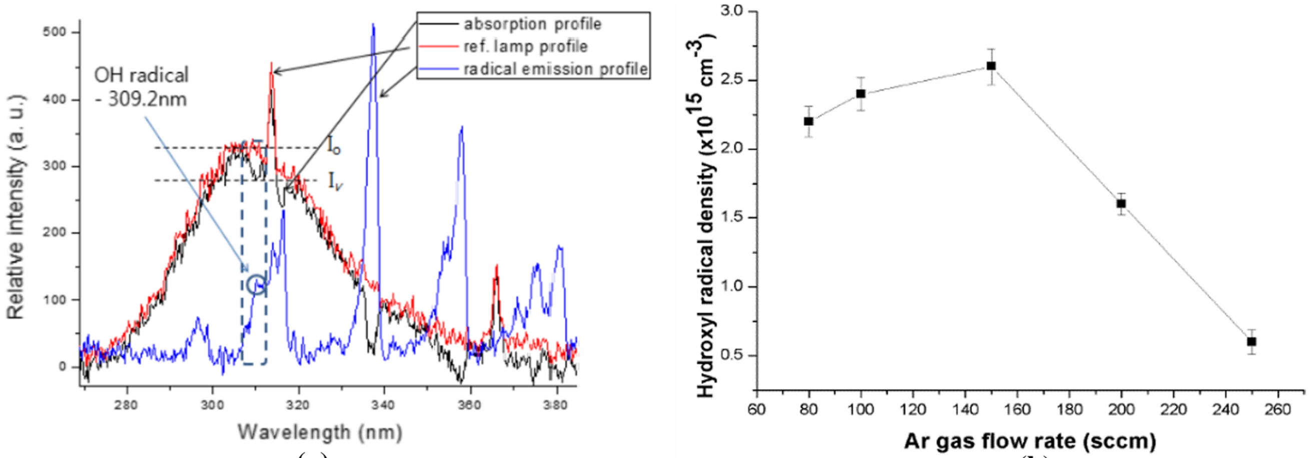

(a)

(b)

Fig. 6 **a** UV absorption profile caused by the OH radical species (black) versus the wavelength. Reference UV lamp profile (I_o) versus the wavelength without a nonthermal atmospheric pressure plasma jet (red). Emission profiles from the plasma versus the wavelength from hydroxyl OH radical species (blue) without UV incidence. **b** Hydroxyl OH radical density on the region of the water surface in contact with the plasma, that is 2 mm above the interfacial region, versus the argon gas flow rate ranged from 80 to 240 sccm [86]

through the atmospheric pressure plasm jet [86]. The UV emission and absorption profiles at 309.2 nm are denoted by circles in the blue line and by the dotted box in the black one, respectively, as shown in Fig. 1a [86]. The transmission ratio (I_v/I_o) for the UV lamp and produced by OH radicals, can be used to estimate the OH density or concentration at the absorbed wavelength of 309.2 nm. Figure 6b shows the OH radical density at 2 mm above the interfacial surface versus the Ar gas flow rate for rates from 80 to 240 sccm under a low electrical power of 15 W with the driving frequency of 22 kHz [86]. In this experiment, the OH density reaches a maximum value of 2.6×10^{15} cm^{-3} for a gas flow rate of ~ 150 sccm, and it rapidly decrease to 6.0×10^{14} cm^{-3} for a flow rate of ~ 250 sccm. Other groups also reported OH densities of $(0.3 \sim 7.5) \times 10^{15}$ cm^{-3} for low contents of water molecules less than 3% for operating gases of He, N_2, and N_2/O_2 mixtures at a microwave frequency 2.45 GHz and at a RF frequency of 13.56 MHz with electrical power larger than 100 W [85, 89, 90].

When a non-thermal atmospheric pressure plasma come into contact with the water surface, the OH density increases drastically to 6.55×10^{16} cm^{-3} at an appropriate applied voltage [86]. For the diagnostics of a nitrogen radical species such as NO_x, many researchers have generally used cavity-enhanced absorption spectroscopy (CEAS) and Fourier transform infrared (FTIR) spectroscopy [91–93]. FTIR is a very useful radical analyzer based on absorption spectroscopy, and a CEAS has been employed in parallel with FTIR [91] for measurement of radical species by including a multipath cavity cell with a high reflection mirror [92] because FTIR spectroscopy has low sensitivity. CEAS has a higher sensitive absorbance of $10^{-7} \sim 10^{-9}$, as compared with $10^{-3} \sim 10^{-5}$ for FTIR. Also, CEAS has a higher selectivity and a faster response time [91–93] and is well adapted for the high-speed dynamics of RONS in a plasma gas. Hence, CEAS is suitable for in-situ analysis and real-time detection [93]. For nitrogen dioxide (NO_2) measurements, the visible BBCEAS method can be used; however, for nitric oxide (NO), CEAS should be used with a mid-infrared laser for diagnostics of infrared-active molecules, whose spectral range is between 3 and 20 µm [94]. The NO_2 absorption can be measured by using ultraviolet and visible light sources such as LED and Xe or Hg arc lamps. The visible absorption band of NO_2 includes the band of the electronic transition in the molecule [95]. However, the vibronic absorption band of these NO species is located around 5.26 µm and the absorption profile can be detected using a quantum cascade laser (QCL). This QCL, which can be adjustable to a specific wavelength of the laser, has been widely used for NO absorption measurements. QCLs have the most suitable characteristics for absorption spectroscopy. For these reasons, NO_2 and NO measurements can be carried out by using the BBCEAS and the QCL–CEAS techniques, respectively. In this review, we report the measurement of NO_2 and NO generated in a nonthermal air plasma jet and obtained using BBCEAS with LED and CEAS with QCL, respectively. For the measurements of the NO_2 and the NO densities, a visible LED (light-emitting diode) whose wavelength is 660 nm and a mid-infrared LD (laser diode) whose wavelength is 5.2386 µm are used, respectively. Radical densities can be calculated from the transmission ratio by using the Beer-Lambert law, which is obtained from the amount of laser intensity absorbed where passing through the gas from the plasma jet in the optical cavity of CEAS [96]. QCL–CEAS has generally been used to measure the absorption of NO radical species. Especially, the

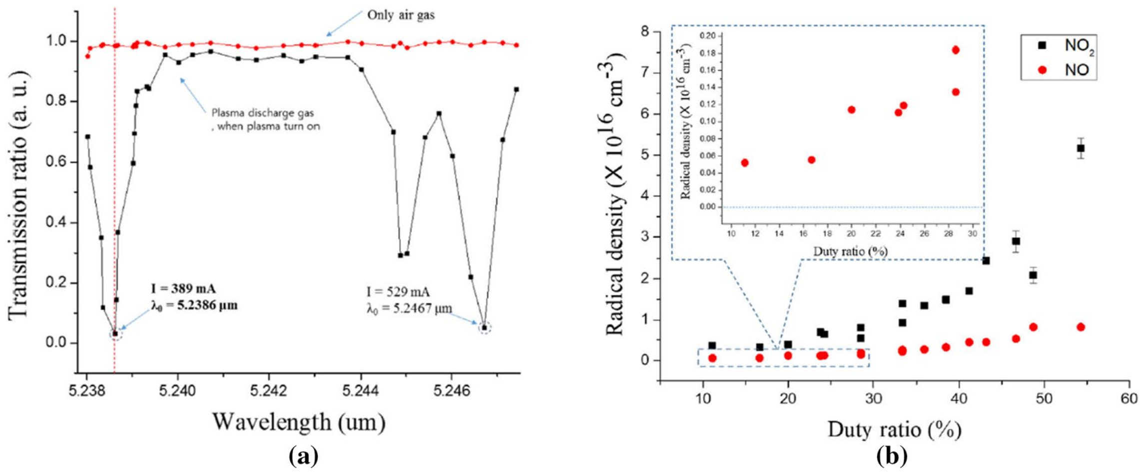

(a) (b)

Fig. 7 **a** Transmission ratio of beam versus wavelength of QCL, and **b** the NO_2 and NO radical density versus duty ratio (%) [96]

NO_2 density has a value of ~ 2.5×10^{16} cm^{-3} in our air plasma jet. The NO density has a value of ~ 4×10^{15} cm^{-3} [96]. The transmission ratio was measured in the range of the QCL's tunable wavelength to find the maximum absorption wavelength of NO. Figure 7a shows the absorption wavelength of 5.2386 µm at the graph's first peak [96]. Figure 7b was the graph for the relation of the NO_2 to the NO radical densities according to the pulse duty ratio [96].

3.3 Measurement of the electron temperature and density

We refer to the nitrogen collisional radiative model of Xi-Ming Zhu and Yi-Kang Pu [97, 98] to obtain the electron temperature and density in an air plasma jet. The processes involve the ground state $X\,^1\Sigma_g^+$ and the excited states $A\,^3\Sigma_u^+$, $B\,^3\Pi_g$ and $C\,^3\Pi_u$ [97, 98]. The main processes are electron impact excitation [97, 98],

$$e + N_2(X) \rightarrow e + N_2(A), \tag{5}$$

$$e + N_2(X) \rightarrow e + N_2(B), \tag{6}$$

$$e + N_2(X) \rightarrow e + N_2(C), \tag{7}$$

where e is the electron, N_2 (X) is a nitrogen molecule in the ground state, and N_2 (A), N_2 (B), and N_2 (C) are excited nitrogen molecules for A, B and C states, respectively [97, 98]. A nitrogen molecule in the A state can collide with are in the ground state:

$$N_2(A) + N_2(X, 5 \le v \le 14) \rightarrow N_2(B) + N_2(X), \tag{8}$$

where v is the vibrational quantum numbers [98]. The excited N_2 (B) can be quenched by collisions with nitrogen molecules in the ground state:

$$N_2(B) + N_2(X) \rightarrow N_2(A) + N_2(X). \tag{9}$$

Also, N_2 (A) under goes wall deactivation [98],

$$N_2(A) \rightarrow^{wall} N_2(X) \tag{10}$$

and the two excited states, $A\,^3\Sigma_u^+$ and $B\,^3\Pi_g$, have the effect of spontaneous emission [98]:

$$N_2(B) \overset{wall}{\rightarrow} N_2(A) + hf, \tag{11}$$

$$N_2(C) \rightarrow N_2(B) + hf, \tag{12}$$

where f is the emission frequency. The processes of Eqs. (11) and (12) cause the spectra of N_2 SPS (second positive system) and N_2 FPS (first positive system) spectra, respectively. Additionally, when the pressure is above 30 mTorr, we have to consider the energy pooling reaction and collision quenching by nitrogen atoms [98]. For the determination of an approximate electron temperature in an atmospheric pressure plasma, we only included energy pooling reaction as follows [97, 99]:

$$N_2(A) + N_2(A) \rightarrow N_2(B) + N_2(X) \tag{13}$$

$$N_2(A) + N_2(A) \rightarrow N_2(C) + N_2(X) \tag{14}$$

Therefore, we can build up the new balance equation for the three excited states included in the energy pooling reaction in the original balance equation of Ref. [98]. In the case of N_2 (A),

$$n_e n_g Q_A + A_B n_B + k_{BX} n_g n_B = k_{wall} n_A + k_{AX} n_v n_A + 2n_A^2 (k_{AAB} + k_{AAC}) \tag{15}$$

In the case of N_2 (B),

$$n_e n_g Q_B + k_{AX} n_v n_A + A_c n_{c+} n_A^2 k_{AAB} = k_{BX} n_g n_B + A_B n_B \quad (16)$$

In the case of N_2 (C),

$$n_e n_g Q_C + n_A^2 k_{AAC} = A_C n_C \quad (17)$$

The n_e, n_A, n_B, and n_C are the densities of electrons and excited states $A\ ^3\Sigma_u^+$, $B\ ^3\Pi_g$ and $C\ ^3\Pi_u$, respectively. The n_v is the neutral gas density for the vibrational temperature and the n_g is the neutral gas density, which depends on the gas temperature. The k_{AX} and k_{BX} are the rate coefficients for the collision processes in Eqs. (8) and (9) [98]. The k_{AAB} and k_{AAC} are the rate coefficients for the process of exiting to upper states $B\ ^3\Pi_g$ and $C\ ^3\Pi_u$ after the collision between excited states $A\ ^3\Sigma_u^+$ in Eqs. (13) and (14) [97–99]. Also, in Eq. (15), the k_{wall} is the rate coefficient of wall deactivation, which is achieved by the diffusion model with the coefficient of wall reflection [98]. The Q_A, Q_B, and Q_C are the rate coefficients for electron impact excitation from the ground state to excited states $A\ ^3\Sigma_u^+$, $B\ ^3\Pi_{g,}$ and $C\ ^3\Pi_u$, respectively [98, 100]. The A_B and A_C are the transition probabilities of excited states $B\ ^3\Pi_g$ and $C\ ^3\Pi_u$ [98]. Therefore, we can obtain three 2nd-order simultaneous equations in three unknowns the excited molecule densities n_A, n_B, and n_C. Equations (15)–(17) can be arranged as follows:

$$2n_A^2(k_{AAB} + k_{AAC}) + (k_{wall} + k_{AX} n_v) n_A + (A_B + k_{BX} n_g) n_B - n_e n_g Q_A = 0 \quad (18)$$

$$n_A^2 k_{AAB} + k_{AX} n_v n_A - (A_B + k_{BX} n_g) n_B + A_c n_c + n_e n_g Q_B = 0 \quad (19)$$

$$n_A^2 k_{AAC} - A_C n_C + n_e n_g Q_C = 0. \quad (20)$$

These excited nitrogen molecule densities can be calculated simply by using a software library called the solve function in MATLAB or Python. In addition, we can express the density of each excitation molecule in terms of these electron temperatures and densities by assigning an arbitrary electron temperature and density to Eqs. (18)–(20). The ratio of molecule densities for nitrogen SPS and FPS can be written as follows [98]:

$$R(kT_e, n_e) = \frac{A_C n_c}{A_B n_B} \quad (21)$$

The values of Eq. (21) have been compared with the measured emission line ratio between N_2 SPS and FPS. N_2 SPS emission lines have been selected at wavelengths of 295.32, 313.60, 315.93, 337.13, 353.67, 357.69, 371.05, 375.54, 380.49, 389.46, 399.84, and 405.94 nm [101]. Also, N_2 FPS intensity was for a wavelength of 654.49 nm [101].

The measured value $R = I_C / I_B$ in Fig. 8 is the line ratio between the one value of twelve lines for N_2 SPS and the line for FPS. Twelve curves of line ratios can be obtained for each arbitrary electron density. The electron temperature for a specific electron density can be obtained by finding the value at the curve of Eq. (21) that matches measured value of the emission line ratio. Therefore, we can express the curve of electron temperatures for arbitrary electron densities. Figure 9 shows the cross point for two curves in the case of $I_{295.32\ nm}/I_{654.49\ nm}$ and $I_{353.67\ nm}/I_{654.49\ nm}$. The determined electron temperature and density are 0.95 eV and 2.5×10^{15} cm^{-3}, respectively, in the Fig. 9. We can calculate the electron temperature and density in a air plasma by using this method.

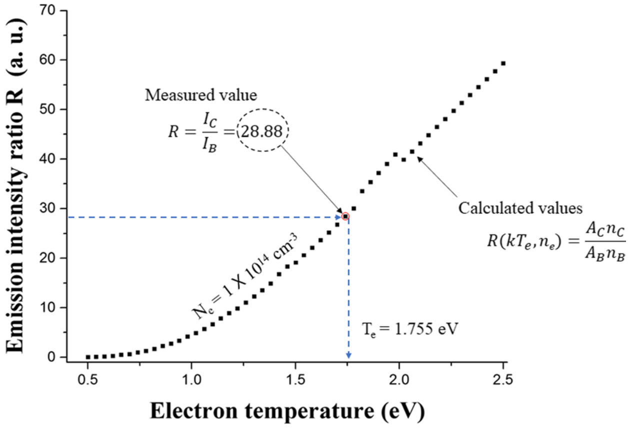

Fig. 8 Electron temperature and density for the line ratio curve between N_2 SPS and FPS

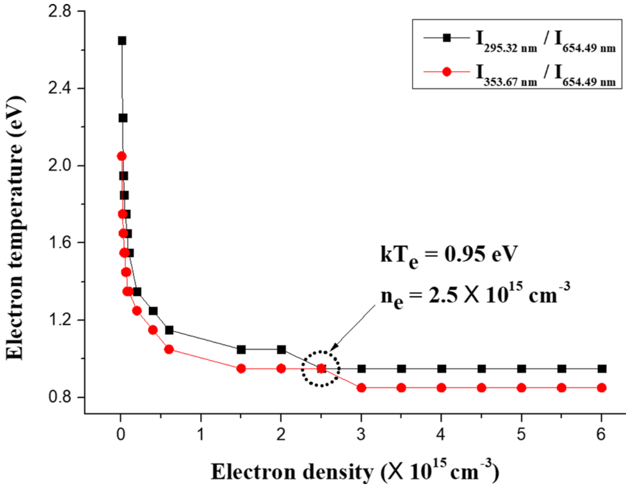

Fig. 9 Curve for finding the crossing point of two curves for the electron temperature and density of $I_{295.32\ nm}/I_{654.49\ nm}$ and $I_{353.67\ nm}/I_{654.49\ nm}$. [101]

3.4 Plasms gas temperature measurement

The plasma gas temperature is fundamentally important for understanding the characteristics of the nonthermal atmospheric pressure (N-DBD) plasma used in most clinical medicines. The Boltzmann distribution of rotational N_2 molecular levels can be used to measure their gas temperature in N-DBD plasmas [102–104] by using the optical emission spectroscopy [102–104]. Most rotational and vibrational gas temperatures can be obtained by using the second positive system (SPS: N_2 $C^3\Pi_u \rightarrow N_2$ $B^3\Pi_g$) [102–104] of N_2 molecular levels rather than the first positive system (FPS: N_{2+} $B^2\Sigma_u{}^+ \rightarrow N_{2+}$ $X^2\Sigma_g{}^+$). Figure 10 shows the transitional energy diagram for N_2 SPS ($C^3\Pi_u \rightarrow N_2$ $B^3\Pi_g$) and N_2 FPS (N_{2+} $B^2\Sigma_u{}^+ \rightarrow N_{2+}$ $X^2\Sigma_g{}^+$) (a) and the optical emission spectra of the N-DBD plasma jet, where N_2 SPS (297–400 nm) and N_2 FPS (550–800 nm), as well as the NO-γ band (213–258 nm) are observed [105]. Vibrational spectra of the N_2 SPS and their magnified rotational spectra belonging to the 0–0 vibrational band are shown in (c) around 337 nm for N_2 $C^3\Pi_u$ (v = 0) → N_2 $B^3\Pi_g$ (v = 0), as indicated by the dotted box.

The intensity $I_{J'J''}$ of a particular rotational transition $J'' \rightarrow J''$ in this SPS is given by [30]

$$I_{j'j''} = A_{v'v''} S_P(J'') n_c \exp\left(-\frac{E_r(v',J')}{kT_{rot}}\right) \tag{22}$$

where $A_{vv'}$ is transition amplitude, $S_p(J) = 6\,J'' - 10/J''$ is the Hoenl-London factor corresponding to the rotational angular momentum quantum number J″, and E_r (υ′, J′) is the rotational energy for vibrational number υ’ and rotational number J’ given by

$$E_r(v',J') = B_v J'(J'+1) - D_v J'(J'+1)^2 \tag{23}$$

where $B_υ$ and $D_υ$ are rotational term for vibrational number υ, $J^{'}$ and $J^{''}$ are the rotational quantum numbers for the transitions (υ = 0, J′)→(υ = 0, $J^{''}$), *k* is the Boltzmann constant,

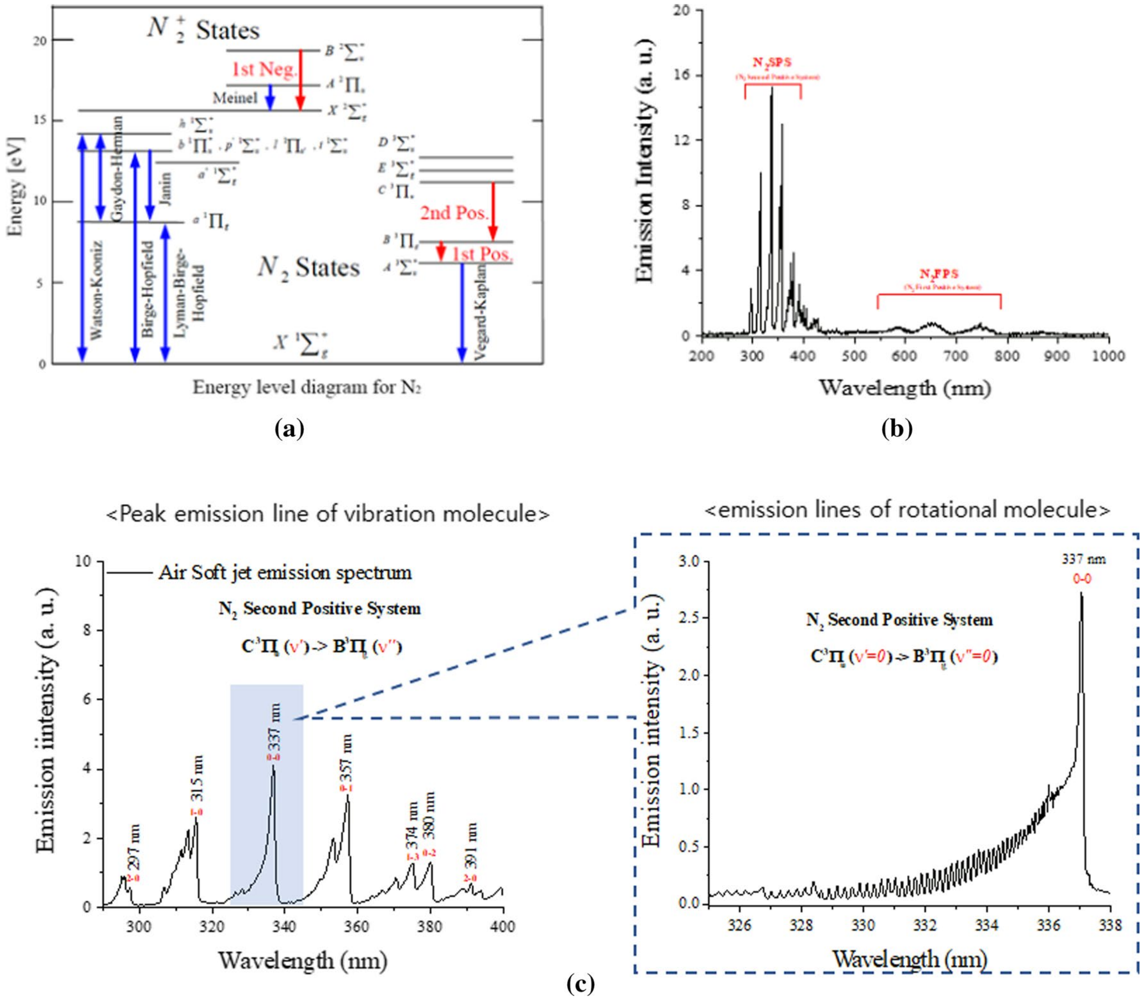

(a) (b)

(c)

Fig. 10 **a** Transitional energy diagram N2 SPS ($C^3\Pi_u \rightarrow N_2$ $B^3\Pi_g$) and N_2 FPS (N_{2+} $B^2\Sigma_u{}^+ \rightarrow N_{2+}$ $X^2\Sigma_g{}^+$). **b** Optical emission spectra of the N_2 SPS and the N_2 FPS. **c** Vibrational spectra of the N_2 SPS and magnified rotational spectrum in the 0–0 vibrational band around 337 nm of $C^3\Pi_u$ ($v = 0$) → $B^3\Pi_g$ ($v = 0$), as in the dotted box (**c**) [105] and T_{rot} is the rotational temperature. For an estimate of the rotational temperature, Eq. (6) can be rearranged as:

$$\text{In}\left(-\frac{I_{J'J''}}{S_p(J'')}\right) = -\frac{B'_v hc}{kT_{rot}} J'\left(J'+1\right)\right) + C \qquad (24)$$

where h is Plank's constant, c is the speed of light, and C is constant. Figure 12 shows a plot of Eq. (24) versus rotational energy given by Eq. (23) with rotational quantum number J'. The rotational temperature T_{rot} of the plasma gas molecules can be determined from the reciprocal value of the slope, $B_v{}' hc/(kT_{rot})$, of the resulting linear plot of the left-hand side of Eq. (24) versus the rotational energy and E_{r}. From this, throughout repeated experiments, the rotational temperature T_{rot} of the plasma gas is estimated to be 807 K for a nonthermal air plasma plume above 1 mm above the surface of the water (Fig. 11).

The vibrational gas temperature can also be estimated by selecting quantum levels of the SPS corresponding to the ν–ν' vibrational band of N_2 ($C^3\ \Pi_u$) (v)—$B^3\Pi g$ (v′). The intensity of a particular vibrational band in this SPS is given by [106],

$$\ln\left(\frac{I_{\nu\nu'}}{\nu_{\nu\nu'} A_{\nu\nu'}}\right) = C - \frac{E_\nu - E_0}{kT_{vib}} \qquad (25)$$

where $I_{\nu\nu'}$ is emission intensity of transition $\nu \rightarrow \nu'$, measured from experimentally, $\nu_{\nu\nu'}$ is the transitional frequency, $A_{\nu\nu'}$ is transitional amplitude, and E_ν is the vibrational energy for quantum number ν given by

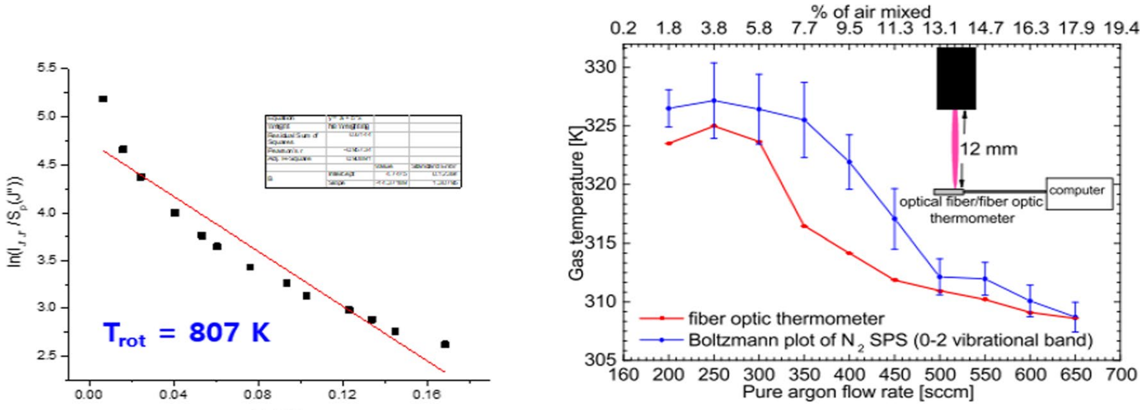

(a) (b)

Fig. 11 **a** Rotational temperature T_{rot} of the plasma gas molecules can be determined from the reciprocal slope of a linear plot of the left-hand side of Eq. (8) versus the rotational energy and E_{r}. This plasma gas temperature is estimated to be 807 K for a nonthermal air plasma plume 1 mm above the water's surface; **b** Estimate of rotational gas temperature at a position of 12 mm below the nozzle of the quartz tube by using a Boltzmann plot of the nitrogen second positive system (SPS) (0–2: vibrational band; peak wavelength: 380.4 nm) (blue liner), which yield 325 K at an Ar flow rate of 250 sccm. Also its comparison with the temperature taken from a fiber optic thermometer (red one) [104]

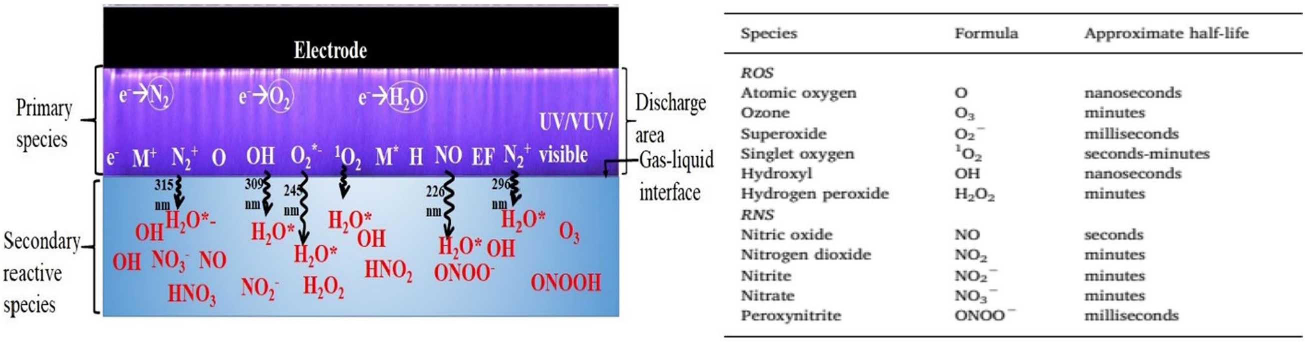

Species	Formula	Approximate half-life
ROS		
Atomic oxygen	O	nanoseconds
Ozone	O_3	minutes
Superoxide	O_2^-	milliseconds
Singlet oxygen	$^1O_2$	seconds-minutes
Hydroxyl	OH	nanoseconds
Hydrogen peroxide	H_2O_2	minutes
RNS		
Nitric oxide	NO	seconds
Nitrogen dioxide	NO_2	minutes
Nitrite	NO_2^-	minutes
Nitrate	NO_3^-	minutes
Peroxynitrite	$ONOO^-$	milliseconds

(a) (b)

Fig. 12 **a** A schematic showing how ions, electrons and neutral particles, as well as UV radiation, contribute to the production of reactive oxygen and nitrogen (RONS) species in gas and water phases during the NBP discharge [21], and **b** their approximate half-lives [21]

$$E_v(eV) = 1.24 \times 10^{-4}\left(\frac{1}{2} + v\right)\left[\omega_e(\mathrm{cm})^{-1}\right]. \quad (26)$$

The vibrational temperature of T_{vib} of the plasma molecules can be determined from the reciprocal value of the slope of the resulting linear plot of the left-hand side of Eq. (25) versus energy difference $E_v - E_{o.}$ From this, the vibrational temperature kT_{vib} of the plasma gas is measured to be 0.2–0.8 eV for nonthermal air plasma plume above 1 mm above the water's surface [104]. Because the density of excited nitrogen molecules in the excited energy bands *C*, *B*, and *A* are up to ~ $10^{17}/\mathrm{cm}^3$, the ratio of excited molecules with both rotational and vibrational temperatures to those of ambient air molecules is estimated to be about 1% where the remaining 99% of most ambient molecules are at room temperature and quickly absorb energy due to the rotational and the vibrational temperatures of these 1% excited molecules, resulting a cool of the temperature, as can be felt when your hand touches this DBD plasma. Hence, we call this kind of plasma as a nonthermal, cold, or cool plasma even though the rotational and the vibrational temperatures are somewhat higher than room temperature.

4 Plasma interaction with water

Most plasma induced reactive oxygen and nitrogen species (RONS) are generated when the NBP interacts with the water's surface or water molecules in the ambient air or within tissue. Here, much physics and chemistry are involved and they are important for understanding the mechanism underlying plasma treatment of wounds or cancer because water is a major component of plasma treatment and it is the simplest hydrated environment in plasma-liquid interactions. Within the simplest water-based model, the mechanisms of why and how NBP generates RONS in water or solution is somewhat solved, but still remain unclear. This is due to the technical difficulty in in-situ measurements of highly reactive molecules generated by the NBP in water, such as the hydroxyl radicals (OH•), superoxide anions ($O_2{}^{*-}$), nitric oxide (NO), peroxynitrite ($ONOO^-$), and other radical species.

Figure 12a represents the schematics showing how ions, electrons and neutral particles as well as UV radiation, generate RONS in gas and liquid phases during a plasma discharge and Fig. 12b their approximate half-lives [21]. Energetic electrons formed in the discharge region can collide with neutral atoms like nitrogen, oxygen, water vapor, etc. and dissociate them. The primary species, OH, NO, O, $O_2{}^{*-}$, $^1O_2$, and $N_2{}^+$, are generated in the discharge region. These primary reactive species [5, 53, 54, 60] in the gas–liquid interface with their half-life times ranging from nano or microseconds (O and OH), milliseconds ($ONOO^-$, $O_2{}^{*-}$), seconds (NO, $^1O_2$), to several minutes (H_2O_2, $NO_2{}^-$, $NO_3{}^-$), emits UV light whose wavelength is in the range from 200 to 400 nm inducing the secondary reactive species in the water. We call this kind of the simultaneous secondary RONS production mechanism in water, it as plasma ultraviolet (UV) photolysis [7, 84–86].

4.1 Plasma ultraviolet photolysis and molecular transport of plasma reactive species

The RONS chemistry induced by the plasma UV radiation originating from NBP is not homogeneous inside the water, where highly reactive molecules are depleted in regions far from the from the water-plasma interface. The physical and chemical mechanisms for generating plasma-induced reactive species in water should be synergistic combination from simultaneous RONS production of plasma UV photolysis and subsequent gas-region RONS diffusion into the water [55, 96–98]. Some significant advances in the understanding of the mechanisms have been achieved and are summarized [107, 108].

The generation OH and H_2O_2 in a plasma UV photolysis with an electrical discharge power of 4.9 W and a driving frequency of 35 kHz, can be visualized inside DI water by irradiating of UV light onto the water surface. The diagnostic methods for these species will be explained. Generally, UV light can be produced by using mercury lamp or any other sources whose wavelength is centered at 306 nm. Terephthalic acid (TA) has been put into the water for visual check of OH production in the water or biosolutions during UV bombardment [109]. Figure 13a confirms that OH species can be generated inside the DI water and PBS, when the liquid's surface with/without quartz filter is placed at 1 mm below the water's surfaces is irradiated with UV light with its energy entered at 4 eV. Because blue color is observed. This UV light can pass the filter and propagate into the water for excitation and dissociation of it, resulting in OH generation. A visual observation of OH species inside the water can be done either by using a red color filter (right side in Fig. 13a) or an irradiation of incandescent light onto the water. No color change for these cases.

Figure 13b shows the generation of H_2O_2 inside the DI water either by UV light or Ar plasma jet bombardment at an electrical power of 4.9 W and a driving frequency of 35 kHz. Here, 0.01 M ammonium metavanadate (NH_4VO_3) is put into the DI water and PBS to observe H_2O_2 production visually when the color changes to orange. Furthermore, the H_2O_2 generation inside the DI water can be confirmed by using a quartz filter when Ar plasma is bombarding the surface. The quartz filter, which is placed just on the water's surface, can screen plasma electrons, ions, and neutral particles so that only the plasma UV emission, which are caused

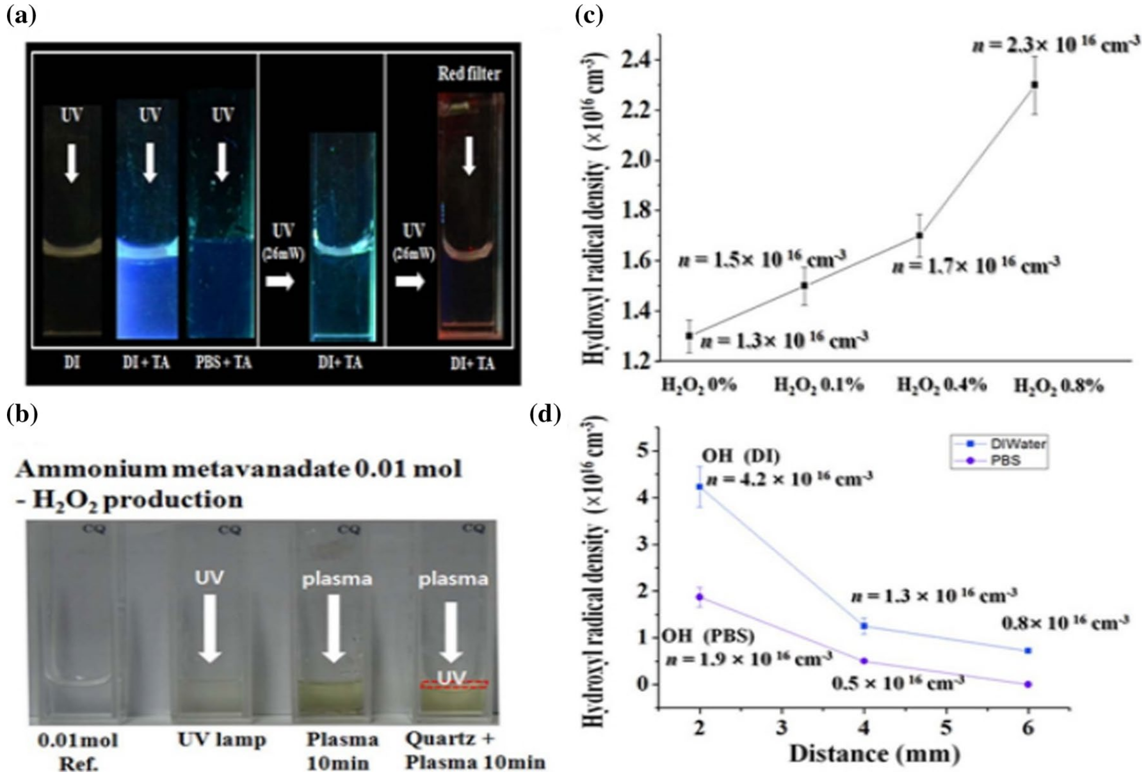

Fig. 13 **a** Visual observation of OH generation inside DI water and PBS with/without TA when a UV mercury lamp is used for the irradiating; **b** visual observation of H_2O_2 generation inside the DI water either by UV irradiation or plasma bombardment of the water with/without quartz filter located just on the DI water; **c** OH density versus the external H_2O_2 concentrations in DI water at a depth of 4 mm for an Ar plasma jet; **d** density of OH versus the depths in the DI and the PBS solutions produced by an Ar plasma jet [110]

from the excited ROS species, can pass through the filter to propagate into the water.

The H_2O_2 and OH species can be generated simultaneously inside DI water and PBS by using plasma UV irradiation. Here the OH density inside the water, produced by plasma UV photolysis, has been observed to have a correlation with the H_2O_2 concentrations. Figure 13c shows there is a strong correlation between the OH and the H_2O_2 concentrations in the DI solution, where the OH density is increased from 1.3×10^{16} cm^{-3} to 2.3×10^{16} cm^{-3} as the H_2O_2 concentration is changed from 0 to 0.8%, respectively. Also, the OH densities (DI, PBS) reach maximum values of (4.2, 1.9)$\times10^{16}$ cm^{-3} and (0.8, 0.1)$\times10^{16}$ cm^{-3} at depth of 2 mm and 6 mm, respectively, below the water's surface, as shown in Fig. 13d at a gas flow rate of 250 sccm [110].

4.2 Plasma parameter characteristics at plasma-water interfacial region

In this section, plasma parameter variations for the interaction between a plasma jet and deionized surface are introduced. Atmospheric pressure Ar, air, N_2 plasma jet and deionized water can be used for this. A cuvette filled with DI water is placed 10 mm below the quartz tube nozzle [111]. Optical emission spectroscopy is performed with a spectrometer with an optical fiber. The optical fiber is installed behind of quartz plate to avoid arcing. A deuterium lamp and a high-resolution spectrometer are installed with lens for absorption spectroscopy of the hydroxyl radical. The optical diagnostics is focused on a plasma bullet located 5 mm below the nozzle.

In this experiment, the length of the plasma jet was observed at least 10 mm from the nozzle regardless of the presence or absence of water. The measured plasma discharge voltage (black line) and current (blue line) are shown in Fig. 14a as functions of time. The rms value of the driving voltage was measured as 2.3 kV, and the plasma discharge current was measured as 10 mA. The plasma bullet current (red line) is measured by Rogowski coil as shown in Fig. 14a and it is found to be 70 mA. The average power dissipation by the plasma discharge (P_{Dis}) can be calculated using the voltage ($v(t)$) and the current ($i(t)$) from the grounded copper tape by using [112]

$$P_{\mathrm{Dis}} = \frac{1}{T}\int_0^T v(t)i(t)dt, \tag{27}$$

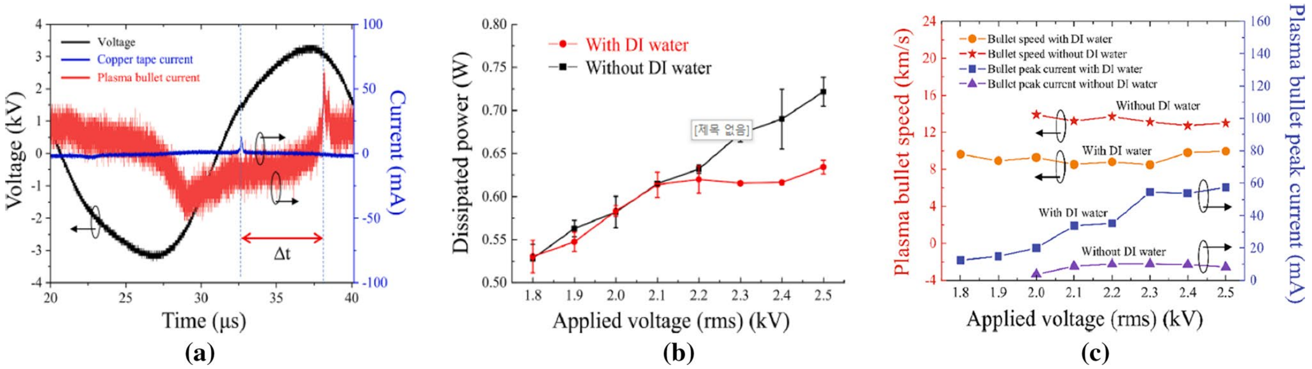

Fig. 14 **a** Plots of the voltage (black line) and the current from the pickup coil (blue line) and Rogowski coil (red line) versus time at 2.3 kV with DI water, **b** dissipated power of Ar APPJ with (red-circle line) and without (black-square line) DI water versus applied voltage, **c** speed of the plasma bullet (red-star line and orange-circle line) and the current from the Rogowski coil (blue-square line and purple-triangle line) with and without DI water versus the applied voltage [111]

where T is the period of voltage. The dissipated power of both with and without DI water are shown in Fig. 14b. They are not very different from each other. However, a significant difference between them appears to occur at voltage above 2.3 kV. Above 2.3 kV, the plasma bullet's current on DI water starts to increase because the DI water's surface serves as a ground. Therefore, the dissipated power in the region of the grounded copper tape region of with DI water is saturated. The velocity and the peak current values of the plasma bullet as functions of the applied voltage are shown in Fig. 14c. A Rogowski coil is used for plasma bullet velocity measurements, and its speed was calculated by time difference (Δt) and distance (ΔL) between the current in the pickup coil and that in the Rogowski coil. The plasma bullet currents with and without DI water are found to be in the ranged from 7.6 to 57.4 mA and 3.6–10.1 mA as a function of applied voltage, respectively, and the plasma bullet's speeds are found to be ranged from 8.5 to 9.9 km/s and 12.7–13.9 km/s as a function of applied voltage, respectively. When a voltage of 2.3 kV is applied, the plasma bullet's current increases as shown in Fig. 14c due to the strong electric field between the plasma bullet and the DI water surface. Thus, the plasma current flows are divided into two parts: the current in the grounded copper tape and the current in the plasma bullet directed to the water surface. The bullet's current is increased with DI water because the DI water's surface serves as a ground that makes the electric field between them stronger. The water vapor for the DI water can reduce the plasma bullet's velocity due to collisions between plasma electrons and water molecules. The chemical reaction for the generation of OH radicals can be explained as the dissociation of water molecules. In the DI water's surface, vaporized water molecules in the gaseous state can increase OH production through collisions with metastable Ar and O atoms and can increase electrons in plasma bullets for interaction [113–115]. The emission intensities of Ar and O as functions of applied voltage provide the evidence of this.

Figure 15 shows optical emissions from a plasma bullet 5 mm below the nozzle. The OH band (306–312 nm), N_2 second positive system (337 nm, 380 nm), O (777 nm) and Ar (696–965 nm) are measured both with or without DI water and the results are shown in Fig. 15a. The intensities of Ar emission, two emission lines at 912 nm and 696 mn, are observed as a function of applied voltage as shown in Fig. 15b. There emission intensities with or without DI water were increased steadily until 2.3 kV. Especially, the maximum value was reached with DI water, which is increased significantly from 2.3 kV. Water vapor due to the interaction between the plasma bullet and the DI water's surface increases collisions with metastable Ar atoms, resulting in a loss of Ar metastable energy. Therefore, when a voltage of 2.3 kV or more is applied, the intensity of Ar emission from DI water decrease. The O atom can be obtained from the dissociation of the O_2 molecule by metastable Ar atoms and electrons [91, 93].

$$\mathrm{Ar}^* + \mathrm{O}_2 \rightarrow \mathrm{Ar} + \mathrm{O} + \mathrm{O} \tag{28}$$

$$e^- + \mathrm{O}_2 \rightarrow e^- + \mathrm{O} + \mathrm{O}(^1\mathrm{D}) \tag{29}$$

The O I emission intensities are measured as functions of the applied voltage and the results are shown in Fig. 15c. These emissions increase with increasing applied voltage with or without DI water, especially with DI water at voltage beyond 2.3 kV. According to the results for the plasma bullet's peak current in Fig. 14c and the Ar emission intensity in Fig. 15b, O atoms appear to arise during the processes described in Eqs. (28) and (29) by the electrons of the plasma bullet and metastable Ar atoms.

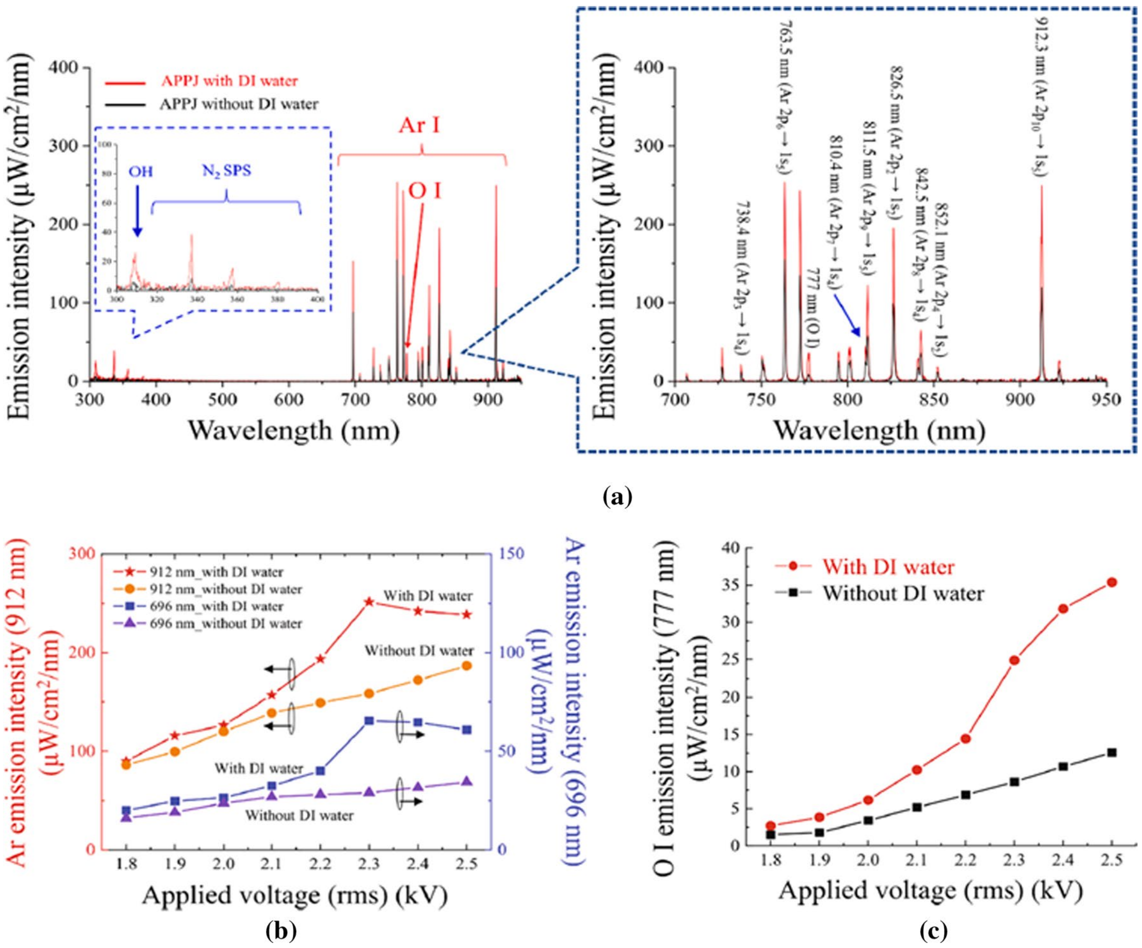

Fig. 15 **a** Optical emission spectroscopy results for a APPJ with (red line) and without (black line) DI water at an applied voltage of 2.3 kV. **b** Metastable Ar emission intensities at 912 nm (red-star line and orange-circle line) and 696 nm (blue-square line and purple-triangle line) with and without DI water as a function of the applied voltage. **c** O I (777 nm) emission intensities with (red-circle line) and without (black-square line) DI water versus the applied voltage [111]

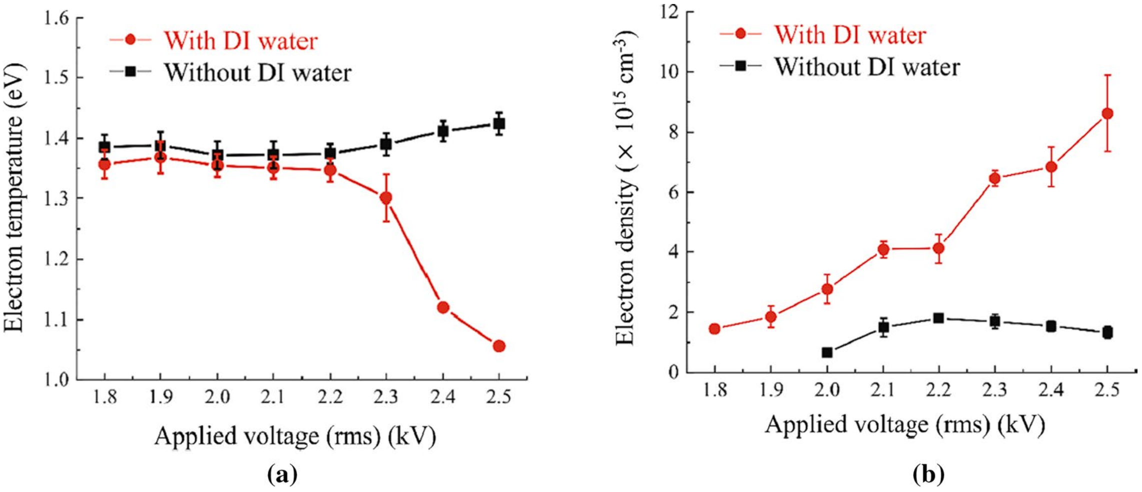

Fig. 16 **a** Electron temperature versus applied voltage, and **b** electron density versus applied voltage [111]

Electron temperature in the plasma bullet has been measured by Ar collisional radiative model and the results are shown in Fig. 16a, and is found to be 1.36–1.06 eV with DI water and 1.38–1.42 eV without DI water. This shows that a decrease in the electron temperature with DI water is caused by a water vapor increase. At a 2.3 kV applied voltage, an increase in the water vapor on the DI water's surface leads to a decrease in the mean free path for electron collision, which leads to electron temperature decrease. At the same time, measured electron densities with DI water are found to be 1.02×10^{15} cm^{-3} to 8.62×10^{15} cm^{-3} with DI water and 6.58×10^{14} cm^{-3} to 1.33×10^{15} cm^{-3} without DI water as shown in Fig. 16b. The increase in the electron densities with DI water can be explained by the presence of water vapor and the following processes [116]:

$$e^- + H_2O \rightarrow H_2O^+ + 2e^- \tag{30}$$

$$e^- + H_2O \rightarrow OH^+ + H + 2e^- \tag{31}$$

In addition, it can be explained by an increase in the oxygen emission intensity, are found in Fig. 15c, due to Eq. (29) caused by an electron density increase.

Figure 17a shows that the absorption profile for OH lines in the range from 306 to 312 nm at a 2.3 kV applied voltage with DI water. The corresponding OH density results are plotted against the applied voltage in Fig. 17b. In this experiment, 309 nm is selected in the absorption spectrum to measure the density of OH radicals. The results obtained with or without DI water increase with the increasing applied voltage. Especially in the presence of DI water, at an applied voltage of 2.3 kV, it rapidly increased to 6.55×10^{16} cm^{-3}, which is about seven times higher than the value at 2.2 kV. This increase in the OH radical with DI water can be explained by dissociation of water molecules by Ar atoms, O atoms and electrons [85, 91–93] as follows:

$$Ar^* + H_2O \rightarrow OH + H + Ar \tag{32}$$

$$O(^1D) + H_2O \rightarrow 2OH \tag{33}$$

$$e^- + H_2O \rightarrow OH + H + e^- \tag{34}$$

The reaction rate coefficients of Eqs. (32)–(34) are 7.8×10^{-10} cm^3/s, 2.0×10^{-10} cm^3/s, and $(1.68T_e - 1.23T_e^2 + 2.19T_e^3) \times 10^{-10}$ cm^3/s, respectively, at a gas temperature $T_g \approx 300$ K [114–116].

Because the emission intensity of metastable Ar atoms in DI water at applied voltage above 2.3 kV is higher than those obtained up to 2.3 kV, the reaction shown in Eq. (31) is one of the main reasons for the increase in the OH densities shown in Fig. 17b. The reaction depicted in Eq. (33) for the generation of OH radicals can be enhanced by increasing the number of O atoms as shown in Fig. 15c. The rate coefficient of Eq. (34) with DI water is reduced from 5.41×10^{-10} cm^3/s to 4.92×10^{-10} cm^3/s by decreasing the electron temperature from 1.35 to 1.30 eV, whereas the electron density increases from 4.12×10^{15} cm^{-3} to 6.47×10^{15} cm^{-3} at applied voltages ranging from 2.2 to 2.3 kV. As a result, the OH radical species can be increased by the reaction depicted by Eq. (34) when a voltage of 2.3 kV is applied.

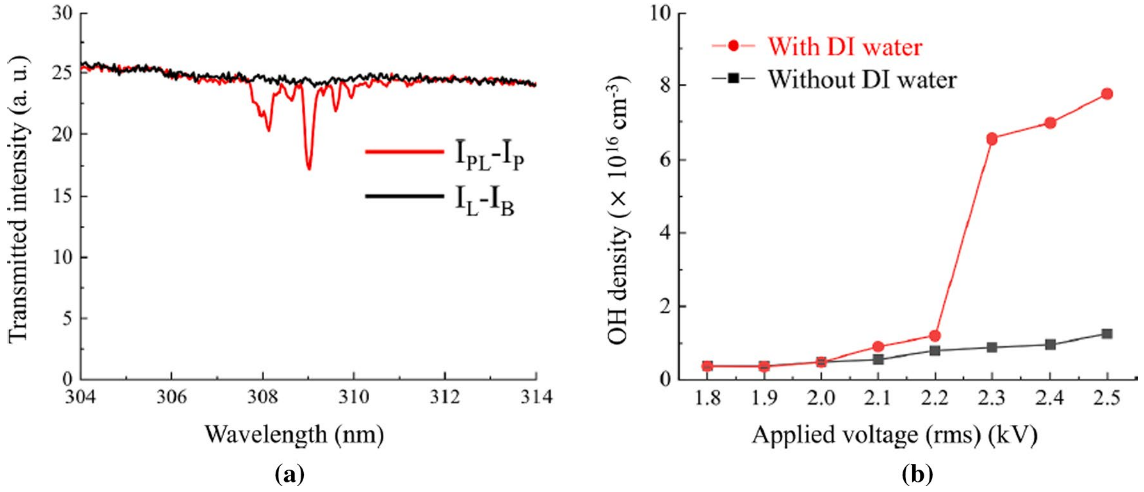

Fig. 17 **a** Absorption profile at 308 nm, and **b** OH densities with/without DI water versus applied voltage [111]

5 International standard for plasma medical equipment

5.1 Measurement of the plasma current

The current between the plasma and the skin is also one of the biological effects of a plasma. Among the conventional medical devices are devices that are expected to have a therapeutic effect caused by an electric current on the patient. Safety limits and measurement methods for the current through the patient are specified in IEC 60601-1-1. The safe value for the patient current given in IEC 60601-1-1 is 100 uA [117]. Sensitive people may feel uncomfortable when sensing the current even when the tolerance is satisfied. The detection threshold is individual and depends on age and gender. From a physiological point of view, the tolerances given in IEC60601-1 do not cause health problems [118].

The leakage current for a soft jet can also measured by among a copper plate target (40 × 40 × 5 mm^3) connected to a test device (UNIMET® 800ST, BENDER), as shown in Fig. 18a, according to the axial distance [119]. As shown in Fig. 18b, the current measured up to only 2 mm from the soft jet nozzle, and no more current is measured beyond 3 mm from the nozzle because the lower measurement limit of the instrument is 1 uA.

5.2 Measurement of ozone and NOx

Atmospheric pressure plasma discharge generates reactive oxygen species (ROS) such as ozone and OH, H_2O_2, and reactive nitrogen species (RNS) such as NO and NO_2 [119]. Reactive nitrogen oxygen species (RONS) generated by a plasma play an important role in biological interaction [120, 121]. Some RONS have toxic properties and require caution in biological applications. Control of RONS produced by using an atmospheric pressure plasma is essential. Safety standards and accurate measurement methods for active species order to ensure the safety of medical personnel and patients when atmospheric plasma medical devices.

In general, ozone and NO_2 are known as air pollutants that have harmful effects on the respiratory systems of humans and animals [122, 123] In the case of ozone, long-term exposure has been reported to be associated with the occurrence of asthma [124]. If the ozone concentration in the atmosphere is more than 0.02 ppm, we can sense the smell. The safety standard recommended by the Ministry of Environment of Korea and ACGIH (American Conference of Governmental Industrial Hygienists) of the United States is 0.05 ppm. It is said that no danger exacts below this standard. If more than 0.44 ppm of NO_2 is generated, people can smell it. NO_2 gas may cause cardiovascular disease when exposed to it for a long time [117]. The safety standard recommended by the Ministry of Environment of Korea and by the ACGIH of the United States is 3 ppm, which should not be exceeded for the health of humans and animals. On the other hand, NO gas is known as an essential substance for maintaining the homeostasis of the human body [125, 126]. In particular, NO is an antibacterial substance that plays an especially important role in the immune system that protects the human body from microorganisms [127].

The measurement method for RONS suggested in the plasma medical device standard is to be from plasma generators are spread. Measured at three locations as shown in the Fig. 19. Figure 19a presents a method for measuring RONS from the front of the plasma generator [126].

Ozone can be measured in accordance with the measurement distance from the nozzle of the soft plasma jet by using a commercial device (200 series, aeroqual), as shown in Fig. 20a. In Fig. 20b, ozone production from the soft plasma jet is seen to be increasing with distance, and it is slightly increased in accordance with the increasing of its off time.

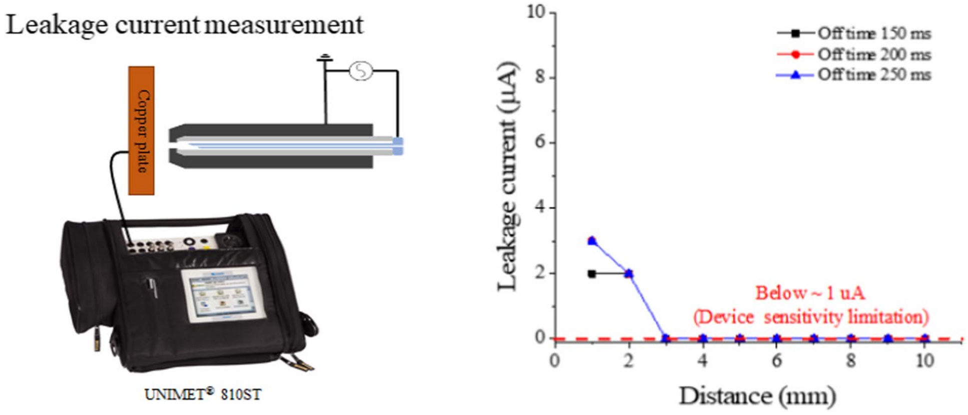

(a) (b)

Fig. 18 Medical requirement limitation measurement: **a** plasma current and **b** plasma current versus distance under several off-time durations in a discharge for a soft plasma jet

5.3 Measurement of the plasma plume temperature at the target

When treating wounds, no damage should be caused by heat from on atmospheric pressure plasma. Therefore, the thermal energy in an atmospheric pressure plasma must be measured. According to IEC 60601-1-1, the temperature of medical devices should not exceed 40 ℃. However, a slight increase in temperature can induce proliferation of living keratinocytes [127]. Therefore, treatment with an atmospheric pressure plasma can actively induce wound healing and tissue regeneration if the temperature of plasma does not exceed 40 ℃. At temperatures, protein denaturation and membrane destruction are well known to occur.

The temperature of the plasma device is shown in Fig. 21a. The results of measuring the temperature according to the distance in the axial direction are shown in Fig. 21b. The temperature profile of soft jet is shown in Fig. 21b

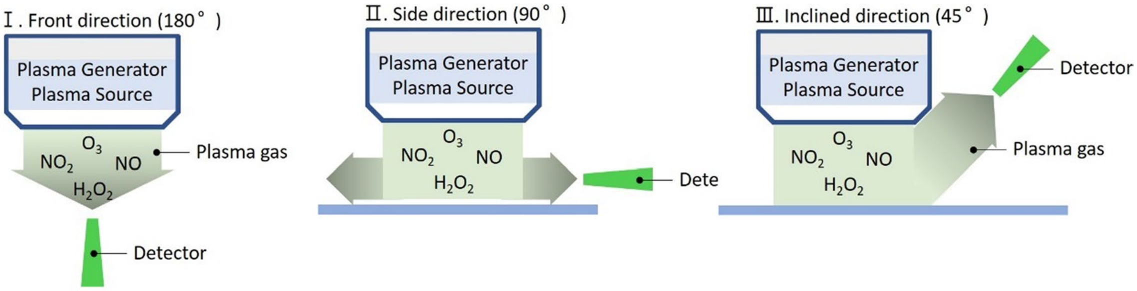

(a) (b) (c)

Fig. 19 Method for measurement the gas emission at different angles **a** 180º, **b** 90º, and **c** 45º

Fig. 20 Medical requirement limitation measurement: **a** ozone measurement and **b** ozone concentration versus distance under several off-time durations in the discharge of a soft plasma jet

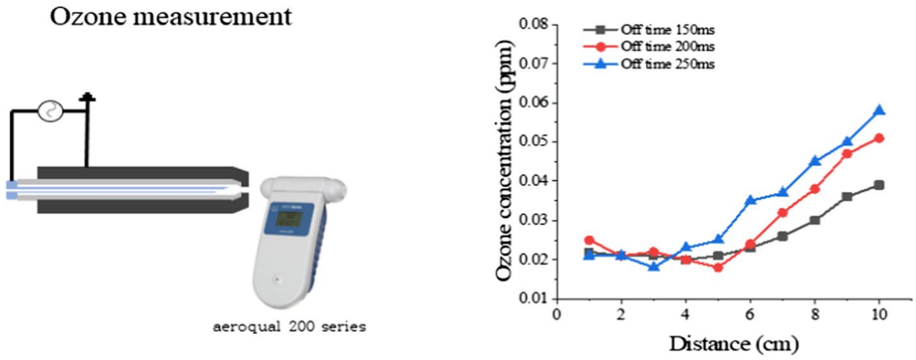

(a) (b)

Fig. 21 Medical requirement limitation measurement: **a** axial temperature measurement, and **b** temperature versus distance under several off-time durations in the discharge of a soft plasma jet

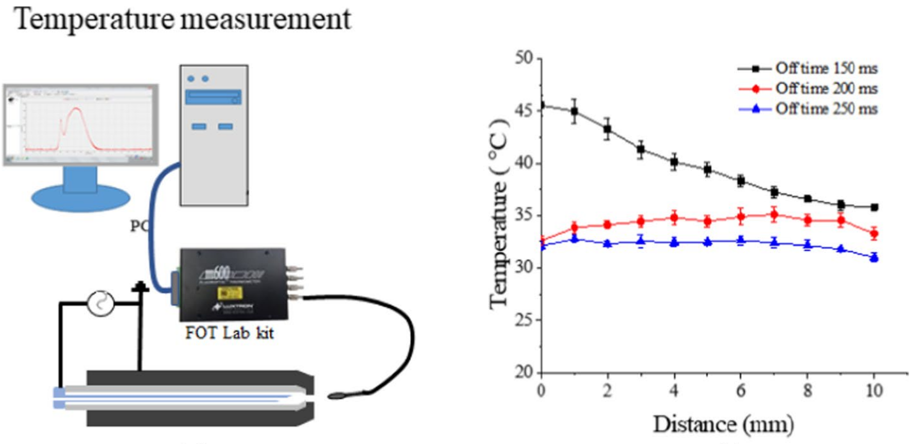

(a) (b)

[128]. As shown in the figure, the temperature is 35–40 ℃ at 7–10 mm from the jet tip. This distance becomes the recommended distance for a soft jet and should be used on patients at this distance to keep the plasma temperature below 40 ℃ [128, 129]. These temperatures are biologically safe and are permitted by IEC60601-1-1.

6 Utilization of plasma bioscience for living health

The healing mechanism of lesion tissues related to bacteria infected and virus-infected living tissues under plasma treatment can be clarified through basic and clinical research by using food-borne and air-borne pathogens. Also, implementing plasma medical devices for these kinds of medical purposes is important. This requires an absolute cooperation system between the two organizations for international standards of food safety and plasma medical devices, joint use of advanced research facilities, joint acquisition of intellectual property rights that will lead the world, and synergy of securing advanced technologies. In particular, the plasma bioscience field shows promising features that could be widely used in the prevention and the treatment of COVID-19 [44, 130], which is pandemic around the world.

6.1 Plasma agriculture and food treatment in fisheries

6.1.1 Plasma agriculture and fishery

Plasmas have an effect on seed germination. From ancient times, there has been a story that grain grows well and harvests are good in summer when there is a lot of thunder and lightning. All of them make sense from the perspective of plasma bioscience. As shown in Fig. 22a, water treated by a “thunderbolt” on tomato seeds, especially seeds sprinkled with plasma-treated water for 15–30 min, grows better and shows strong pathogen resistance [23–34]. This is due to an increase in the growth hormone and the pathogenic hormone resistance of plants when seeds are exposed to a plasma [26]. In addition, Staphylococcus aureus (S. aureus) has strong resistance and is widely present in air and soil.

It lives on the skin of humans and animals, is easily contaminated through food, and can cause food poisoning and sepsis. As shown in Fig. 25b, The NBP-DBD surface plasma can control *Staphylococcus aureus* (*S. aureus*) and *Bacillus cereus* (*B. cereus*) bacteria in dried anglerfish, which are related to food poisoning [131]. More than 90% of *S. aureus* and *B. cereus* killed when treated for about 30 min; the effect is about 99% after about 1 h [131]. The important point here is that the color coordinates do not change significantly, and even the shape, taste, aroma, and overall water solubility of dried anglerfish are not significantly affected. Therefore, in the case of dried fish, if a large-area DBD-NBP plasma is irradiated for about 30 min, a sterilization rate of 90% or more can be expected, and no side effects are expected to occur. Therefore, plasma treatment of dried seafood can be considered during production, processing, and distribution under conditions that sufficiently ensure food safety. Likewise, plasmas can be actively used in the production, storage and distribution of agricultural and livestock products.

6.2 Inactivation of antibiotic-resistant superbacteria

In everyday life, people visit hospitals to receive medical treatment when they are sick or to hospitalized family members. They can be infected indoors for no reason while waiting for treatment, or during visits to the hospital. Also, they can even be infected with antibiotic-resistant superbacteria in the hospital, putting them at risk. Infection with

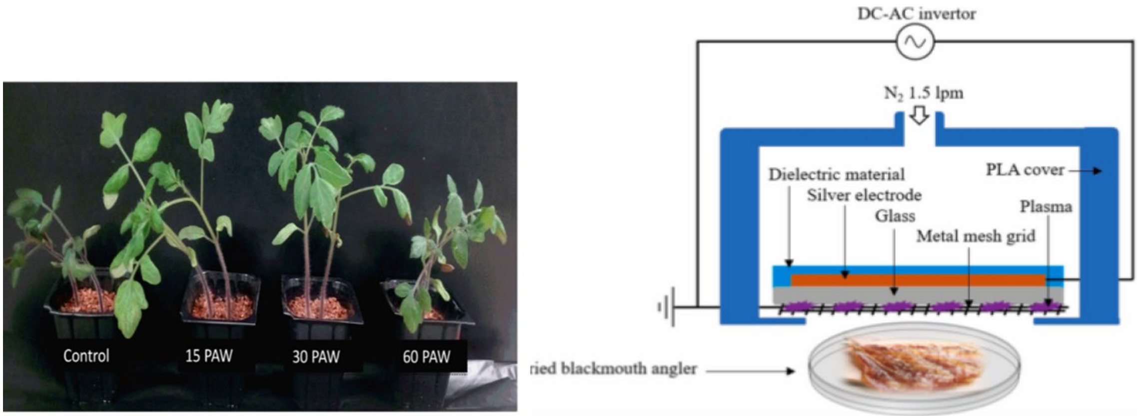

Fig. 22 **a** Effect of treatment using NBP on the germination and growth of tomato seeds [26]. **b** Schematic view of DBD-NBP plasma treatment on the reduction of *S. aureus* and *B. cereus* on black mouth angler fish [131]

antibiotic-resistant superbacteria, which has a resistance to methicillin as well as penicillin, is becoming a serious problem. Antibiotic-resistant bacteria include penicillin-resistant *Staphylococcus aureus* (PRSA), gentamicin-resistant *Staphylococcus aureus* (GRSA), and methicillin-resistant *Staphylococcus aureus* (MRSA). Antibiotic-resistant bacteria, which are difficult to treat, have been reported to be inactivated by using a nanosecond pulsed plasma or large-area DBD-NBP plasma. [45].

As shown in Fig. 23a and b, the expression levels of MRSA resistance genes ecA, mecI, mecRI, and femA before and after plasma treatment are compared using the Q-PCR (quantitative real time polymerase chain reaction). The expressions of all resistance genes are known to be remarkably reduced, which is related to changes in the composition of the cell wall. The genes of multidrug resistant bacteria (PRSA, MRSA and GRSA) are significantly reduced after 20 min of plasma treatment, allowing the superbacteria to be controlled very nicely. At this time, peptidoglycan is revealed to have been oxidized by affecting the molecular bonds of carbonyl groups in the bacterial cell wall due to the synergistic action of reactive oxygen and pH [45]. As shown in Fig. 24a and b, when a nanosecond pulsed plasma with an energy per pulse of 0.1 J or less is used, the shock wave is revealed to play a major role in deactivating bacteria. Its detailed mechanisms can be revealed through studies of the interactions between plasmas and liquids.

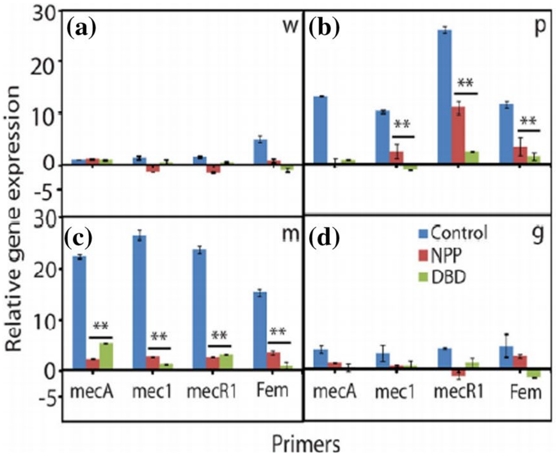

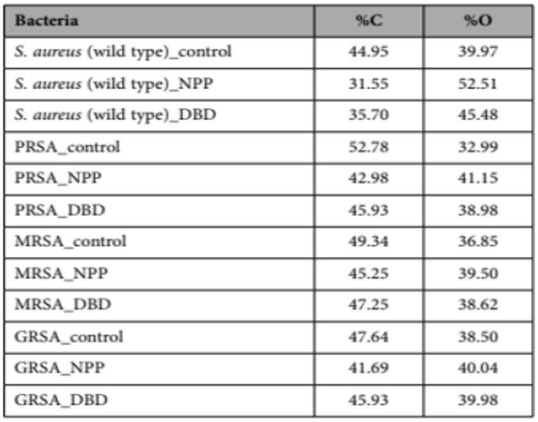

Bacteria	%C	%O
S. aureus (wild type)_control	44.95	39.97
S. aureus (wild type)_NPP	31.55	52.51
S. aureus (wild type)_DBD	35.70	45.48
PRSA_control	52.78	32.99
PRSA_NPP	42.98	41.15
PRSA_DBD	45.93	38.98
MRSA_control	49.34	36.85
MRSA_NPP	45.25	39.50
MRSA_DBD	47.25	38.62
GRSA_control	47.64	38.50
GRSA_NPP	41.69	40.04
GRSA_DBD	45.93	39.98

Fig. 23 **a** Gene expression analyses after NPP and Ar-DBD-NBP treatment: **a** wild type S. aureus, **b** PRSA, **c** MRSA, and **d** GRSA [45]. **b** Experimental composition of bacteria with or without plasma treatment, as obtained using XPS [45]

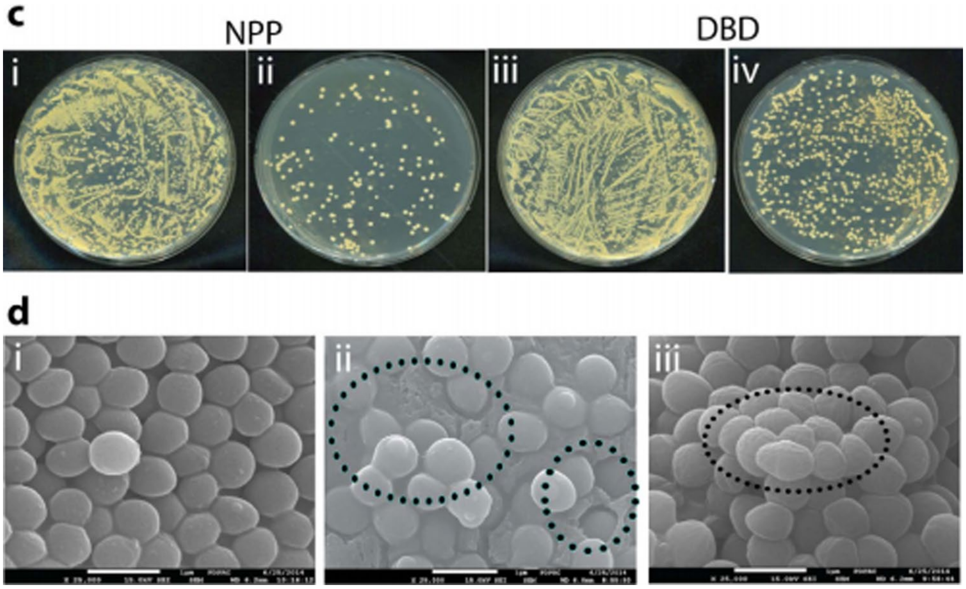

Fig. 24 [Top: **c**] Colony of *S. aureus*: (i) wild type, (ii) after NPP treatment; (iii) wild type, (iv) after Ar-DBD-NBP treatment [45]. [bottom: **d**] SEM images of the *S. aureus*: (i) wild type, (ii) after NPP, and (iii) after Ar-DBD-NBP treatment [45]

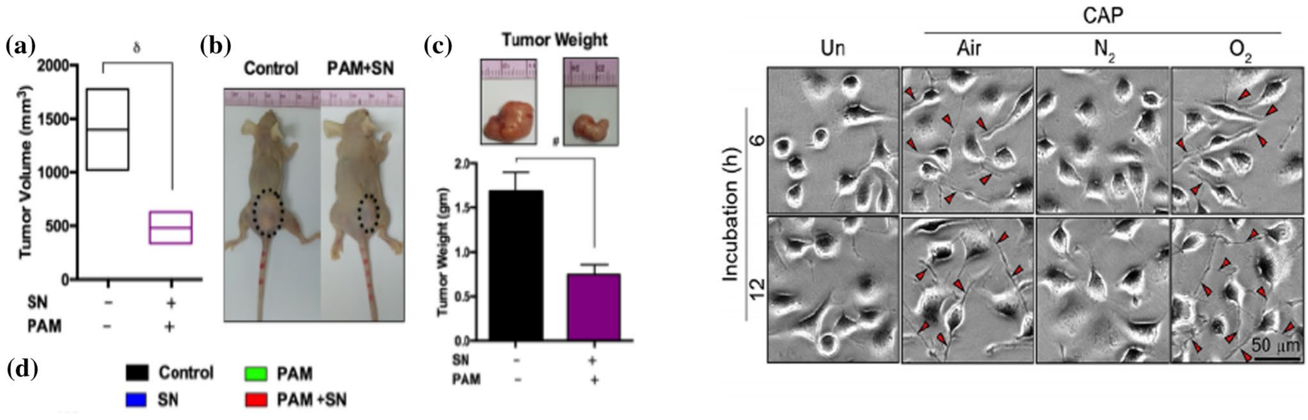

Fig. 25 **a** Anti-tumor effect of silymarin nanoemulsion (SN) and plasma activated PBS treatment in a mice model. **a** Changes the tumor volume in xenograft mice models. **b** macroscopic observation of a control group and dual treatment of NBP-activated PBS and SN to nude mice group bearing subcutaneous tumors on the right hind flank and **c** tumor sizes [132]. **b** Representative SEM images of mouse neural differentiation by air, N_2, and O_2 NBP synapses formed in response to a 1 min exposure of NBP (scale bar = 50 um) [20]

6.3 Apoptosis of intractable cancer cells and healing of degenerative brain diseases

Plasmas can be used to cure intractable cancer lesions through changes in DNA, apoptosis and cell cycle control proteins through the interaction of NBP or nanoparticles with them. Figure 25a shows the results of simultaneous treatment of a silymarin nanoemulsion (SN) and phosphate buffered saline (PBS) treated with air DBD-NBP in xenografted mice with G361 skin cancer cells. Reactive oxygen radicals in cancer cells are increased by about 3 times compared to cells without plasma treatment, and active nitrogen is increased by about 2.5 times, which damages the DNA of cancer cells and reduces the size of the tumor. [132] In addition, malignant proteins, such as plaque and tau knots of beta amyloid (A_β) protein, and the Lewis body, a variant of alpha-synuclein, will accumulate in neurons in the cerebral cortex, which may become a normal protein again by promoting immune activation and enhancing the antioxidant function of nerve cells through the interaction of plasma reactive species. In particular, when atomic oxygen (O) in the reactive species existing in air, nitrogen, and oxygen NBP plasma are used their neurons are differentiated as shown in Fig. 25b, which is applicable to degenerative brain diseases such as Alzheimer's disease (dementia) and Parkinson's disease [20].

In addition, breast cancer cells that have recently developed resistance to anticancer drugs involve an epiimmune mechanism with active oxygen of DBD-NBP, and the sensitivity of anticancer drugs has been stably restored so that and anticancer drugs can be used continuously. In addition, the plasma itself can target cancer tissues by restoring and promoting the immune system [133].

6.4 Plasma application in cancer treatment approach

In the last several years, non-thermal plasmas have been found to be highly effective tools for the delivering reactive species to cancer cells in vivo or in vitro. Interesting initially the NTP was not designed to promote cancer cell death by inducing oxidative stress-mediated cell death through reactive species generation. However, over time, developments in plasma diagnostics and technology methods have provided targeted delivery of controlled mixtures of various reactive species to tumor cells to regulate many events critical to their malignant behavior and eventually to stimulate preferential cancer cell apoptosis and metastasis by taking advantage of short-lived and long-lived species such as H_2O_2 [134–136]. Plasmas have very low gas temperatures, which make them suitable for direct use on living tissues [137]. In mid-2019, the first clinical trial of a plasma was approved by the FDA and was used to extend the 2-year survival of a 33-year old patient in a late stage pancreatic cancer [138]. Notwithstanding the increased number of favorable reports, which shows the plasma efficiency and selectivity against a wide variety of cancer cells, [137, 139], the functions of different plasma-induced effects in cancer-cell malignant transitions, including drug sensitization remain largely unknown. Prominently, triple-negative breast cancer cells lacking required receptors for clinical purposes have increased endogenous ROS levels and are therefore, more sensitive compared to receptor-positive breast cancer cells, signifying the importance of plasmas in sensitizing these cells more efficiently over another breast-cancer subtype [140, 141]

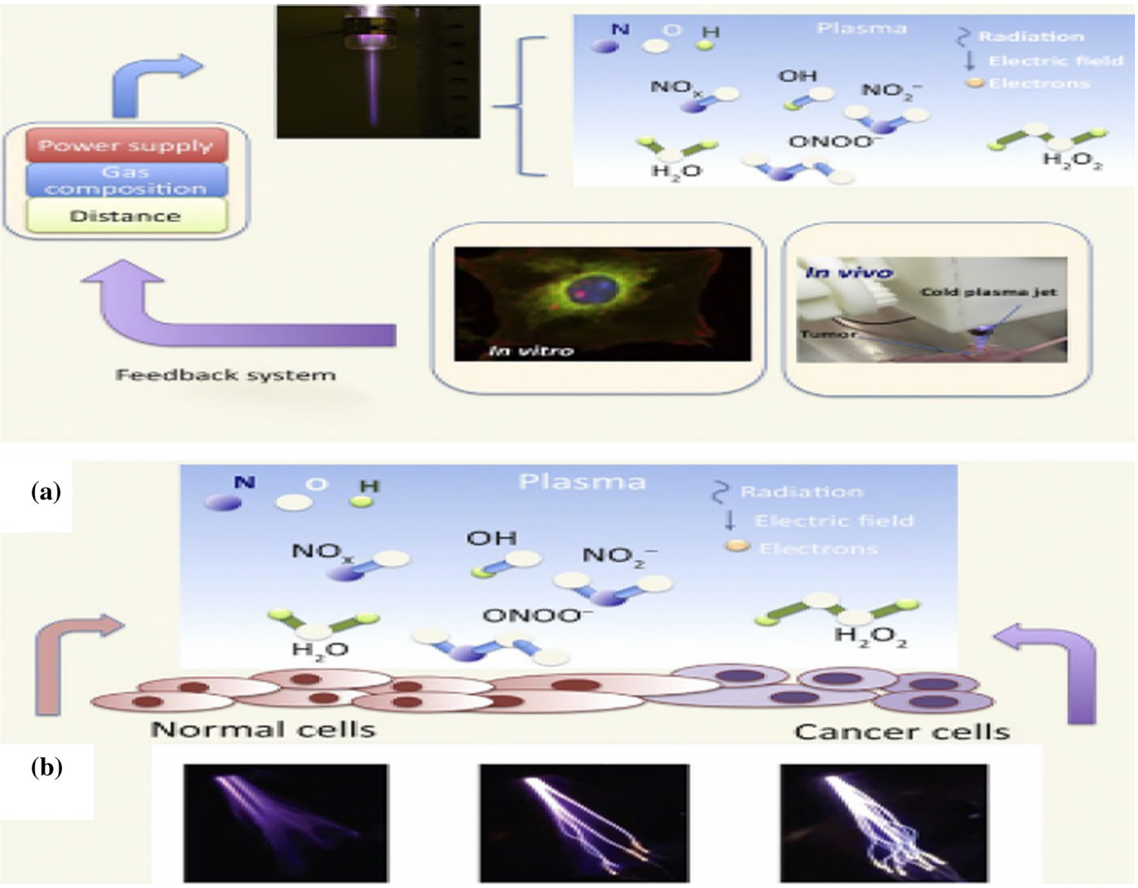

Fig. 26 Adaptive plasma. **a** Concept of an adaptive plasma. Cold plasma treatment in vivo or in vitro will trigger differing responses in cancer cells and normal cells. The signal based on these responses will be measured, recorded, and analyzed by using a plasma system. Through the feedback system, the chemical composition will be modulated through changes in the power supply, the gas composition, and the distance between the plasma source and the cells. **b** Plasma self-adaptation-based self-organization and pattern formation [142]

Keidar et al. suggested that the use of a plasma could be efficient for targeted cancer cells treatment due to its flexibility in managing the plasma-generated reactive species chemistry, which eventually responses to control the molecular events involved in cancer progression (Fig. 26) [141]. Plasma are well known to promotes preferential cancer cell killing in a dose-dependent fashion, i.e., from cell growth arrest to necrosis/apoptosis [143, 144]. Also, cancer cells were found to be more sensitive to endogenous H_2O_2 rather than exogenous H_2O_2 over normal counterparts, possibly due to the presence of a high catalase concentration on their cell surface, as tumor cells have a high local concentration of a catalase on their cell surface which defends them against exogenous H_2O_2 [145, 146]. Singlet oxygen generated from a chemical reaction between peroxynitrite and H_2O_2 activates a high number of singlet oxygen in cancer cells which triggers intracellular reactive-species mediated apoptosis signaling [147]. In addition, ozone, besides H_2O_2 and singlet oxygen has been implicated as another key player in the underlying mechanism of plasma-mediated cancer apoptosis [148].

Apart from apoptotic cell death, recently, plasmas have been shown to be efficient for inducing immunogenic cell death (ICD) in melanoma and lung cancer cells [149, 150] in vitro and in colorectal cancers in vivo, [151] where short-lived reactive species such as nitric oxide and hydroxyl radicals are found to be active constituents [142]. This study provides the first confirmation that plasmas have potential for cancer immunotherapy which can be applied clinically. H_2O_2 is an essential player in oxidative-stress induced apoptosis [152, 153], but not in ICD [18]. Recently, Kaushik et al. reported that the growth of cancer cells could be inhibited when they are co-cultured with plasma-stimulated macrophages via iNOS TNF-α release. Interestingly, plasmas do not reduce immune cell viability after exposure. These findings reveal that plasma generated reactive species could activate cytotoxic macrophages for cancer cell death [154]. In an additional study, the authors found that plasma

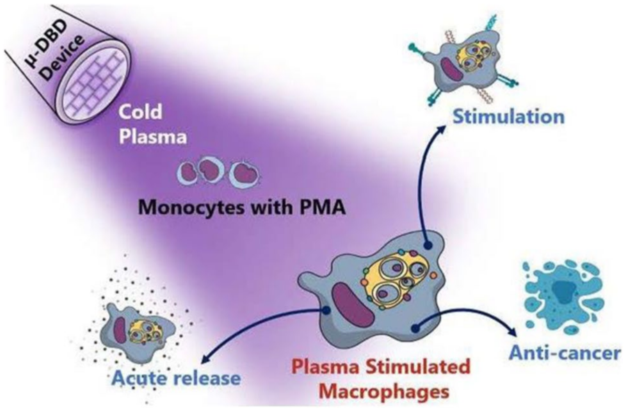

Fig. 27 Non-thermal plasma induced immune cell activation for ICD induction [155]

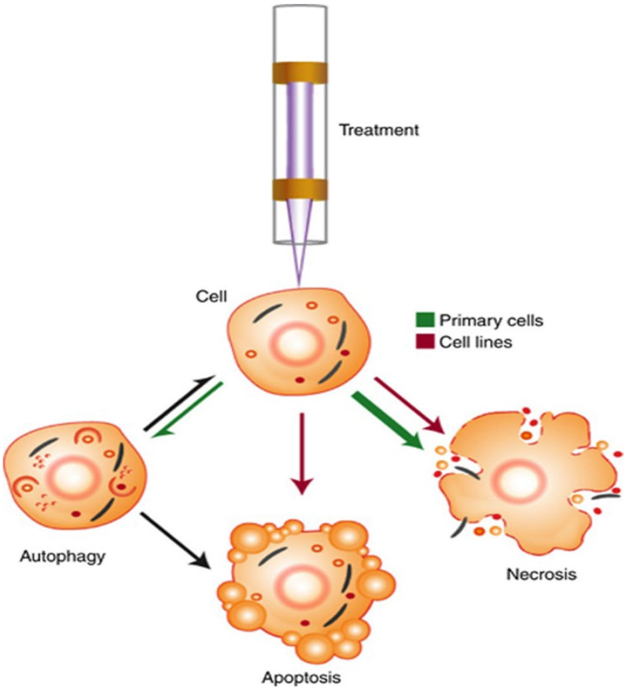

Fig. 28 Overview of cellular response mechanisms following LTP treatment [159]

exposure could successfully differentiate pro-inflammatory macrophages, which supports anti-cancer immune responses in resistant tumor cells (Fig. 27) [155]. Reports in the literature have indicated that plasma application may be helpful targeting immunosuppressive cancers by modifying the pro-tumor microenvironment.

Recently, a group of researchers showed the capability of plasma treatment for necrosis induction by means of primary fibroblast cultures isolated from human oral tissue [156]. Moreover, a plasma can cause another form of cancer cell death, named senescence, by initiating a calcium influx in skin cancer cells [157]. Several studies highlighted the importance of dose given by the plasma to cancer cells because when the level that healthy can cells tolerate is exceeded, cells themselves can be killed too (Fig. 28) [158, 159]. Plasma can act as switch to control the fate of cancer cells due to its dose-dependent characteristics under certain circumstances which makes its use favorable as an anti-cancer approach. In another way, plasma exposure which is a cocktail of chemical reactive species, and physical effects (heat and UV), can be utilized to determine the condition of healthy cells that human encounter in their daily life, such as normal tissue and transition events during carcinogenesis similar to ionizing radiation used in medical field.

Usually, in advanced cancer stages, oncologists prefer radiotherapy widely for malignant and invasive tumors; however, normal tissue side-effects and developed resistance reduce the success rate of radiotherapy in cancer patients. Recently, plasma treatment has been revealed to restore cell sensitivity to traditional therapeutic modalities, such as temozolomide and tamoxifen, in resistant gliomas [160] and breast cancer [161] cells and to slow integrin signaling pathways that facilitate chemo- and radio-resistance in different cancer cells (Fig. 29) [162]. Instead, researchers also tried to improve plasma effect on cancer selectivity by targeting cancer cell metabolism. In order, Kaushik et al. used the combination approach of plasma and 2-Deoxy D-glucose (2-DG) to destroy blood cancer cells, where effective anti-cancer effects were achieved at low doses of plasma. This study claims that the addition of 2-DG enhances the plasma efficiency by targeting the cancer glycolysis pathway, which eventually leads to cancer cell apoptosis by intrinsic pathways [11]. They further extended their study and tested the effect of silymarin nano-emulsion and plasma co-treatment on skin cancer cells. Remarkably, this dual-treatment approach impaired the epithelial-mesenchymal transition (EMT) and cancer stem cell maintenance observed as in vitro and in vivo [132]. Cancer cells believed to be are extremely heterogeneous, which makes them susceptible or resistant to particular treatments, including radiotherapy and chemotherapy. Since plasma generates a mixtures of various chemical species and particles, it can target different cellular biomolecules or associated pathways in this heterogeneous cancer cell population. This property of a plasma makes it potentially more effective over traditional methods.

Moreover, plasma selectivity can be achieved by using functionalized nanomaterials having specific target recognition in cancer cells [163]. Using this concept, to analyze plasma activity induced using nanomaterials, Kaushik et al. investigated the effects of a combination of PEG-coated gold nanoparticles and a plasma on the tumor metastasis. It is claimed that cancer cell growth was inhibited by deactivation of the PI3K/AKT signaling pathway, along with reversal of EMT, as was observed by a delay in tumor growth in

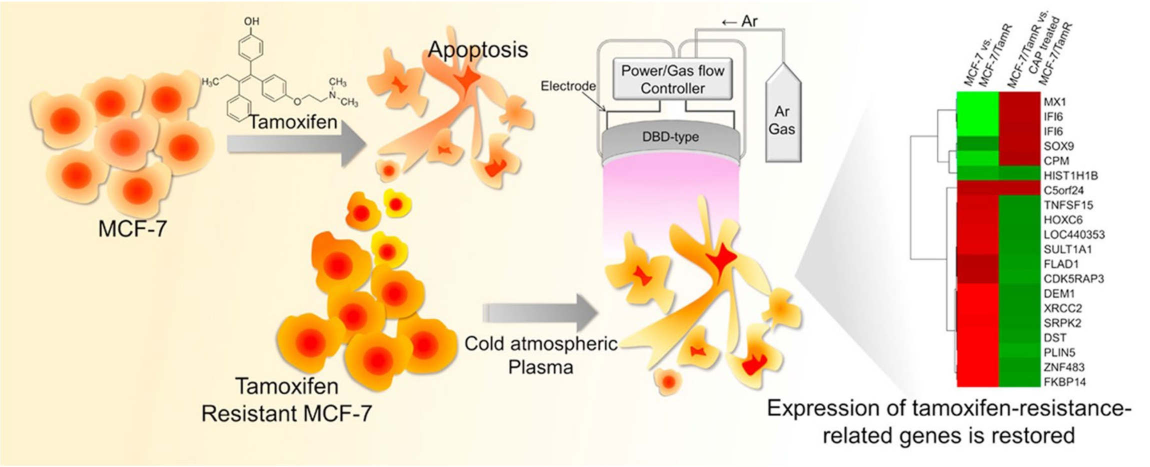

Fig. 29 Treatment of tamoxifen resistant MCF7 breast cancer cells by using plasma and gene expression analysis to uncover mechanism related to for plasma-induced cancer cell sensitization [161]

a tumor xenograft mice models [66]. Having a successful plasma approach in nanoparticle formulation, Linh et al. fabricated polydopamine-functionalized gold nanoparticles, avoiding the use of added toxic chemicals. Specially, plasma treatment reduced the reaction time essential for the synthesis of these particle unlike traditional chemical methods. Worth mentioning is that these synthesized have increased cellular uptake and cytotoxic effect, as seen in breast cancer cells, which emphasize the significance of plasma–fabricated PDA-GNPs for inhibition of cancer cell growth through targeted delivery inside the cells [164].

For cancer treatment, plasmas can be generated using various plasma sources or alternatively can be administered indirectly to cancer cells in the form of a liquid such as a plasma-activated medium (PAM), making it a quite flexible tool for clinical purposes [165]. In direct plasma treatment, only confined treatments are achievable. Nonetheless, the PAM selectivity against cancers is subjective, such as cell type as compared to direct plasma treatment [166, 167]. Many scientists have proposed that cancer-cell death induced by PAM largely relies on the combination of NO_2- and H_2O_2 [168, 169]. Given the short incubation times of plasma-oxidized solutions, such as Ringer's lactate, sodium chloride, and PBS, such solutions can be beneficial in improving the efficacy of in vitro experiments [170, 171]. In another study, repeated treatment with PAM by intraperitoneal injection was found to reduce the mice tumor growth as seen by MRI, leading to improved survival rate. This group suggested that due to the nominal side effects of such plasma-oxidized solutions, they are suitable therapeutic tools for treating advanced stages tumor [171]. However, further conclusions are definitely needed to determine whether PAM treatment can prevent tumor relapse by using xenograft mouse models [74]. For clinical safety assessment of plasma, Isbary et al. conducted ex vivo experiments using human skin tissues, where a 2 min plasma treatment did not induce DNA damage to human cells [172]. Currently, clinical testing of plasma safety and efficiency is being considered regularly in treatments of chronic cutaneous ulcers in phase I or II trials. Plasma treatment was feasibly tolerated in most cases, without any frequent adverse effect [173]. Our primary perceptions are not restricted to only cancer research using plasmas. Plasma can also be advantageous for the treating other deadly human diseases such as neurological disorders [174].

6.5 Cellular mechanism of NBP as plasma treated liquid for cancer

NBP has been reported to have a selective killing effect on targeted cancer cells with minimal effects on regular cells that act by generating reactive oxygen species (ROS) and reactive nitrogen species (RNS). In previous study, we assessed the effects of a non-thermal air soft jet plasma on the U87 brain cancer by using the physicochemical and biological (PCB) correlation between the RONS cascade and MAPK/PI3K/AKT signaling pathway, which resulted in apoptosis [175, 176]. The results showed that the soft jet plasma significantly inhibited cell proliferation, induced cell cycle arrest, inhibited survival pathway and induced apoptosis pathway in U87 cells (Fig. 30).

Both gaseous and liquids plasmas are acts on this concept. It is possible to capture the plasma particles by generated gas type of plasma into liquid. Comparison of the features of NBP and NO water as a plasma-treated liquid (PTL) for cervical cancer cells [177]. PTL was reported to have a cytotoxicity for various cancer cells like NBP, and both use the same cellular mechanisms to induce DNA damage and apoptosis. We have been developed a

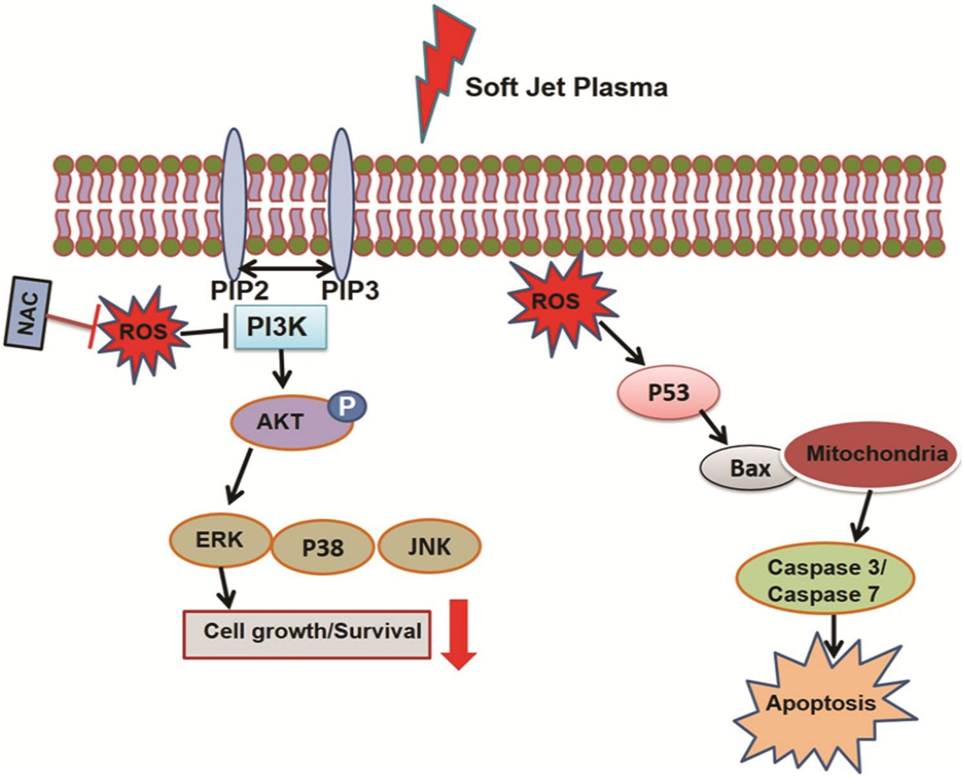

Fig. 30 Diagram of cellular mechanism underlying NBP in brain tumor

microwave jet plasma system producing nitric oxide for aqueous soluble NO (nitric oxide) in distilled water at room temperature. The concentration of nitric oxide could controlled by using the gas flow and the microwave power. According this results, we sought to explore the effects on cervical cancer cells of NO water as PTL on cervical cancer cell line compare with DBD-NBP. Therefore, although some technical challenges remain to be addressed, unlike radiation, which has been thoroughly studied, DBD-NBP and NO-PAM have the potential to be new application for effective and safe clinical trials (Fig. 31).

In-vivo studies have revealed that NBP-PTW showed anticancer effects on chemo-resistant lung cancers, and on non-small cell lung cancer (NSCLC). The effect were similar to these aspect of a cancer drug, gefitinib drug, in the chemo-resistant NSCLC model [178]. Gefitinib is a epidermal growth factor receptor-tyrosine kinase inhibitor (EGFR-TKIs) and has been shown to have significant benefits for treating NSCLC. The anticancer activities of PTW seems to be involved in inhibiting proliferation and in angiogenesis and enhancing apoptosis in tumor cells (Fig. 32). Interestingly, PTW contributes to an enhanced immune response and improved cachexia in the model.

The NBP as a gas stage and a liquid stage is shown to have systemic application (oral administration) and apical application (direct administration) in the treatment of cancer cells subsequently it can be useful tool for clinical trial to improve of cachexia and immunostimulation.

6.6 Regenerative medicine for stem cell modification by using the NBP

The NBP can use tissue engineering to stimulate stem cells and scaffold [179]. When discharging the NBP to stem cells, differentiation of stem cells without other stimuli induced by bone cells has been reported. The NBP generates fast ions, and free radicals and then immediately reacts with surface of molecules subsequently occur the oxidation/reduction reaction. In stem cells, can induce differentiation by reactive species by providing various stimuli to the cells.

Also, the NBP can stimulate to osteogenic initiation without osteogenic induction molecules like ascorbic acid on MC3T3-E1 cells [180]. MC3T3-E1 is an osteoblastic precursor cell line from C57BL/6 mouse calvaria tissue. MC3T3-E1 has stimulated the osteogenic differentiation when treated with ascorbic acid and beta-glycerophosphate to forming osteogenic molecules such as alkaline phosphatase (ALP) osteocalcin (OCN), osteopontin (OSP), collagen type 1 (COL1), and Runx2.

We hypothesized that the non-thermal plasma can stimulated osteogenic initiation without osteogenic induction molecules like ascorbic acid. Here we claim the effect on the osteogenic potential of NBP on stem cells, such as human bone marrow stem cells (hBMSCs) and human periodontal ligament stem cells (hPDLSCs) [181]. The stem cells were cultured and then treated with NBP with or without induction medium. We evaluated the differentiation rate of cells

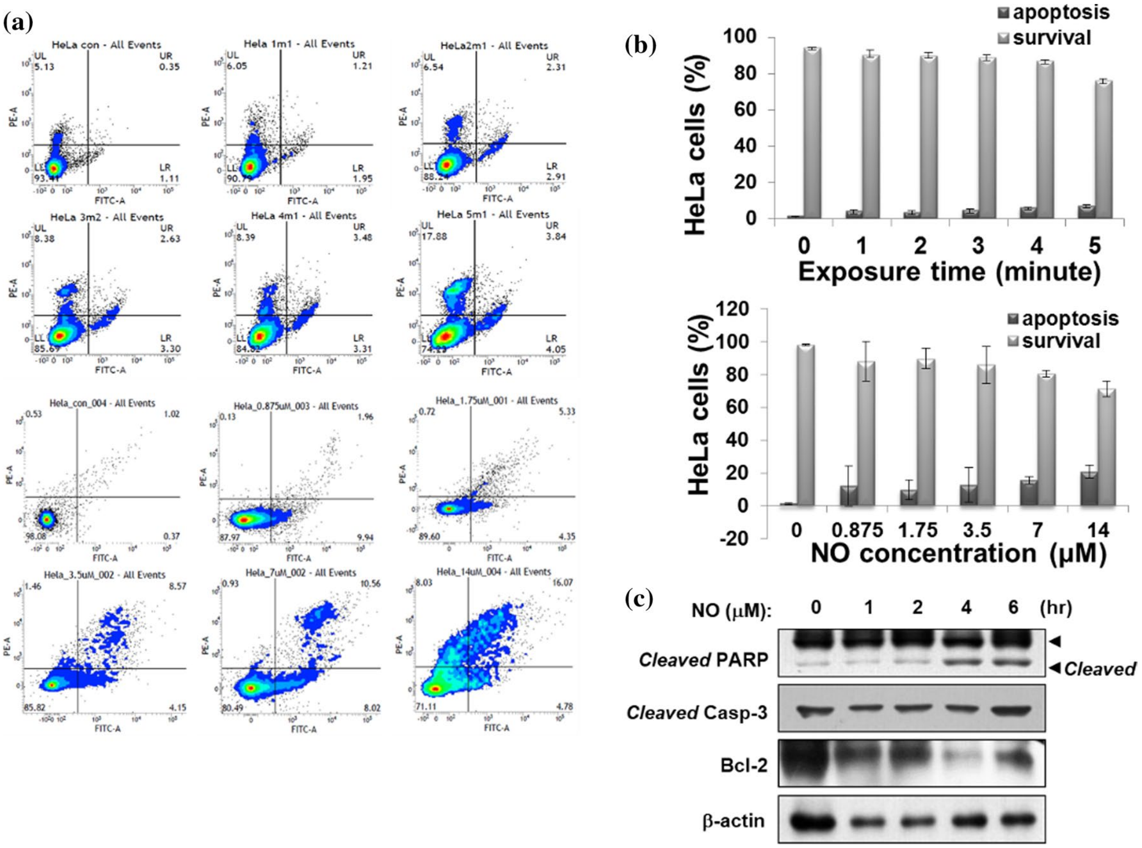

Fig. 31 Apoptosis of HeLa cells after NBP and NO-PAM treatment. HeLa cells were treated with NBP for different times and with NO-PAM different concentrations. Dot plots in **a** and histograms in **b** for NBP (upper) and NO-PAM (lower) showed that both longer-time NBP treatment and higher-concentration NO-PAM treatment could induce more Hela cell apoptosis, compared with control group. **c** Western Blots performed to confirm the apoptosis effect of NO-PAM inducing apoptosis in Hela cells with NO concentration of 7 μM, and incubated for 1, 2, 4, and 6 h after treatment

by using real time PCR. It increased BMSCs and PDLSCs. Nonthermal plasma treatment without osteogenic induction medium. The osteogenic differentiation marker, OCN, osterix, Runx2 and ALP expression level was increased in those cells. PDLSC cells were treated with a plasma for different time and then characterized by real time PCR. As depends on treated time, it was clearly observed increasing the OCN, Runx2, COL1 by the plasma treatment.

Our study demonstrated that NBP has the ability to induce osteogenic differentiation of hMSCs. Moreover, we found that MSCs from different tissue sources had different responses to NBP-induced osteogenesis, while hPDLSCs had more compliance and controllability than hBMSCs. More importantly, we have deeply studied the reason for the effect of NBP, and we believe that NBP treatment activates ROS-sensitive molecules, p38 MAPK, and that the activated p38 MAPK further stimulates antioxidants for cellular homeostasis and FoxO1 expression to modulate osteogenic differentiation in hPDLSCs (Fig. 33). Our study reveals for the first time the mechanisms underlying NBP and hPDLSC, osteogenic differentiation, which lays the foundation for the application of NBP in bone tissue regeneration and engineering the NBP can induce new bone. In additional, it may be use combinations of conventional therapeutic treatment, as well as new approaches, to target tissue for bone regeneration.

6.7 Plasma application to COVID-19 (SARS-COV2: Coronavirus 19)

SARS-COV-2, or COVID-19, originated in 2019, has now spread worldwide at an alarming rate, thus infected about several million people, and has caused about millions of deaths, with an approximate death rate of 2.2%. In addition, confirmed cases continue to spread infected in Asia, US, Europe, Africa and all around the world. Now, many kinds of vaccines against COVID-19 have been developed, and some of countries are now vaccinating people to achieve herd immunity. Viruses play an important role in the global ecological environment, such as the carbon cycle of the sea [182]. On the other hand, pathogenic viruses infect tens of millions to hundreds of millions of animals each year on the

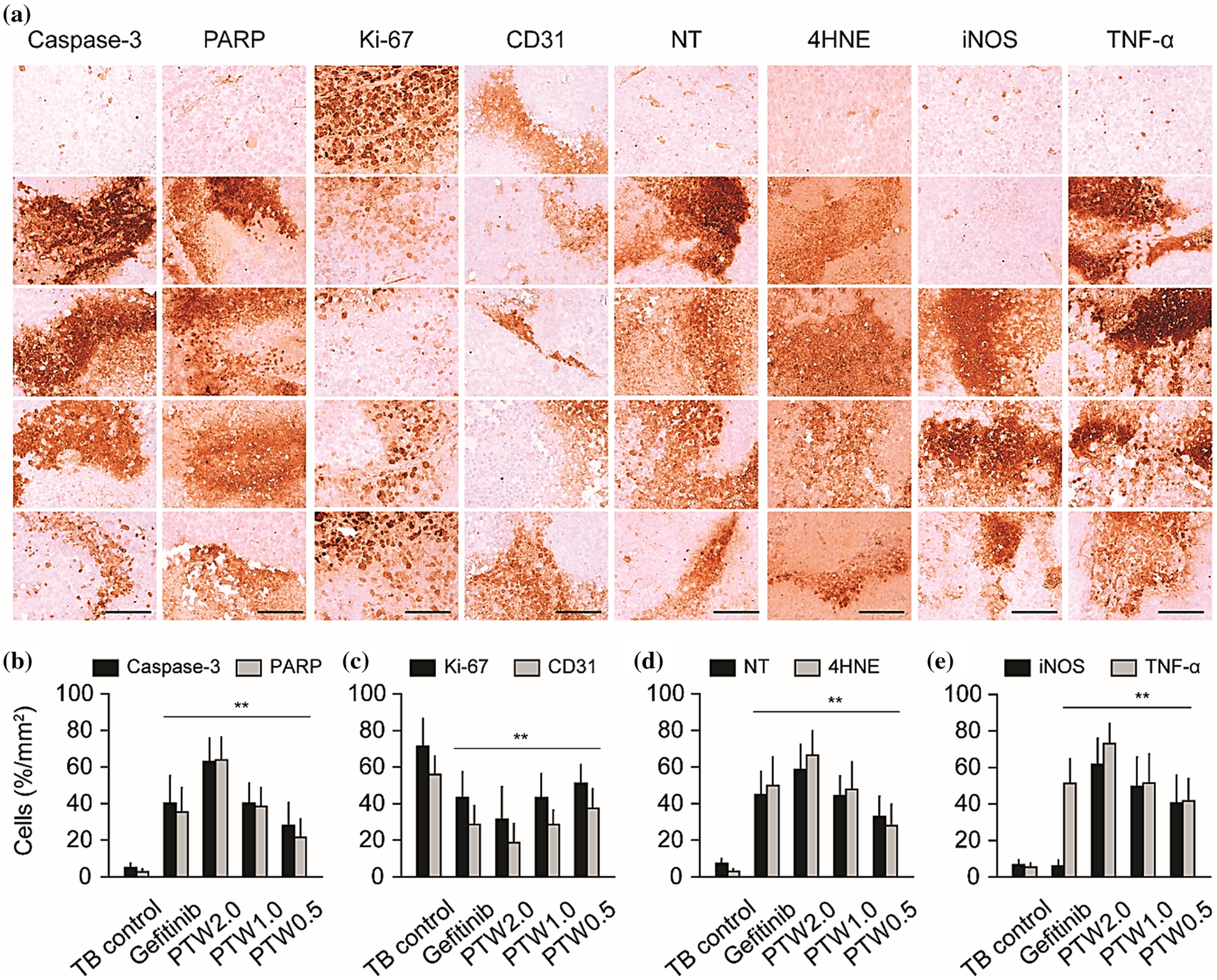

Fig. 32 Immunohistochemistry in tumor mass. Tumor tissue was stained for caspase-3, PARP for apoptosis, Ki-67 for cell proliferation, CD31 for angiogenesis, nitrotyrosine (NT) and 4-hydroxynonenal (4HNE) for oxidative stress, and iNOS, TNF-α for immune response (**A**). The percentages of immune-reactive cells are shown in (**B**–**E**) [178]

Fig. 33 Schematic diagram for plasma effects on precursor cells for osteogenic differentiation through FOXO pathway stimulated by p38 signaling

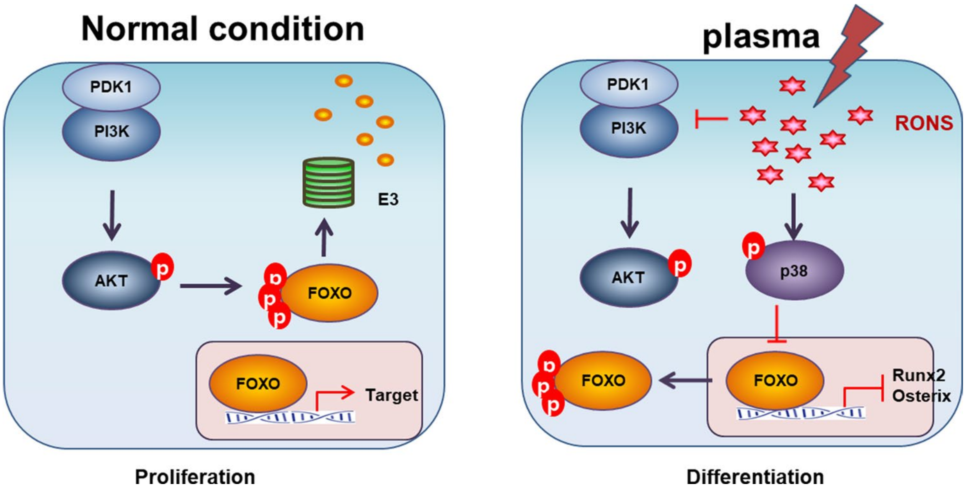

planet or infect people. This has resulted in a decrease in crop yield and a loss of many lives. Therefore, inactivation of harmful viruses is an essential and very important issue for human health.

In the last 2-decade, three coronavirus (CoV) outbreaks (SARS 2002, MERS 2013, SARS-COV-2 2019) have occurred. SARS-CoV-2 (COVID-19), a major threat to human health and the world economy, has a high homology of 80% with SARS-CoV and 50% with MERS-CoV, all of which are beta-coronaviruses. Therefore, the future threat virus (named CoV-X) likely be a variant of it. Despite repetitive pandemics such as SARS-CoV, MERS-CoV, SARS-CoV-2, etc., we do not have date from of a preemptive comparative analysis of the virological, immunological and pathological characteristics of the strains or viruses that have not yet spread from animals to humans. With the proposition that the coronavirus continues to repeat the pandemic of human infection, the follow-up work of emergency investigations on SARS-CoV-2 might be a potential help to find risk factors and treatment options for a future pandemic. Preemptive investigations on plasma treatment of coronavirus strains or other host-derived species are needed in future.

SARS-COV2, which originated in Wuhan, China in December 2019, has now spread globally at an alarming rate and other variants of concerns are emerging after every few months, still infecting about million of people, and causing about several deaths by an approximate death rate of more than 2%. In addition, variant positive cases continue to spread in the US, Australia, Brazil, Europe, Africa, Asia and other part of world. Viruses have been dominate for the over billions of years on the earth [182], and many types of them exist and have adapted, evolved, and mutated according to the situations.

Viruses are important microbial predators that influence global biogeochemical cycles and drive microbial evolution, although their impact is often under appreciated. Viruses play an essential role in the carbon cycle of the sea [182]. On the other hand, pathogenic viruses infect millions of human and animals every year on the earth. Thus, the inactivation or suppression or control of pathogenic viruses is a critical and important issue for the health of humans and animals. The inactivation or suppression of a virus can be successfully processed using reactive oxygen and reactive nitrogen in a plasma [183]. Figure 34 shows a plasma consisting of electrons, ions, and cocktail of reactive oxygens and nitrogen species at room temperature, that can inactivate various type of viruses. The reactive species cocktail interaction with viruses causes damages to genetic material such as DNA or RNA and proteins of the viruses, as shown in Fig. 34. In the case of nucleic acid, a plasma can damage DNA and RNA, can reduce cell replication, and can inhibit the proliferation of viruses due to the enzyme activity caused by oxidation of lipids and proteins. SARS-COV-2 virus and its variant strains, which are highly pathogenic, can also be inactivated by using a nonthermal plasma, which is considered a new hope for virus treatments [44]. This virus-based research area is still relatively young and started about two decade ago, almost coincident with the perspective of plasma bioscience researches [183–185].

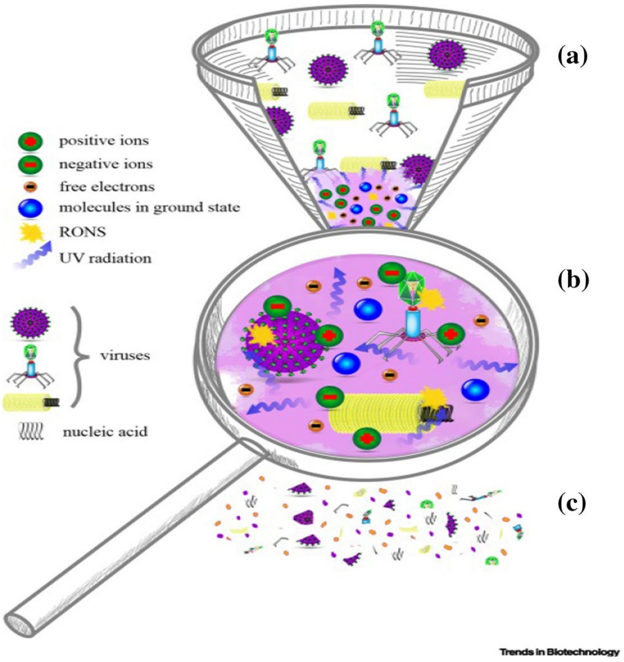

Fig. 34 Inactivation of viruses using a nonthermal biocompatible plasma. **A** Various types of viruses (morphologically different) treated with nonthermal plasma. **B** Magnified plasma properties responsible for virus inactivation. ROS, RNS, UV radiation, and ions and electrons (charged particles) are the most essential constituents for virus inactivation. A NBP can target both viral nucleic acid and proteins. **C** After NBP treatment, the virus proteins, and the genetic materials such as DNA, RNA are degraded to non-infective particles that cannot affect its hosts. [44]

In the early 90 s, ozone was known to be able to inactivate the virus. Due to many safety issues for using only ozone gas, many groups are conducting their investigations on the inactivation of viruses by using other eco-friendly ionized gases while maintaining ozone some level. NBP plasmas have been commonly used in several areas for microbial inactivation or decontamination. Recently, a few plasma research groups initiated preliminary investigations on corona viruses by using various kinds of plasma devices and treatment procedures [44, 46, 48, 49, 186–188]. Recently, viruses were shown to be using plasma exposure and plasma activation liquids such as water, media, buffers, clinical solutions etc. Figure 35 shows the effectiveness of plasma jets in removing corona viruses from the surfaces of objects [187]. Both plasma activated water and plasma treatment showed inactivation of viruses in an exposure dose dependent manner, and investigations suggested no side-effects with no

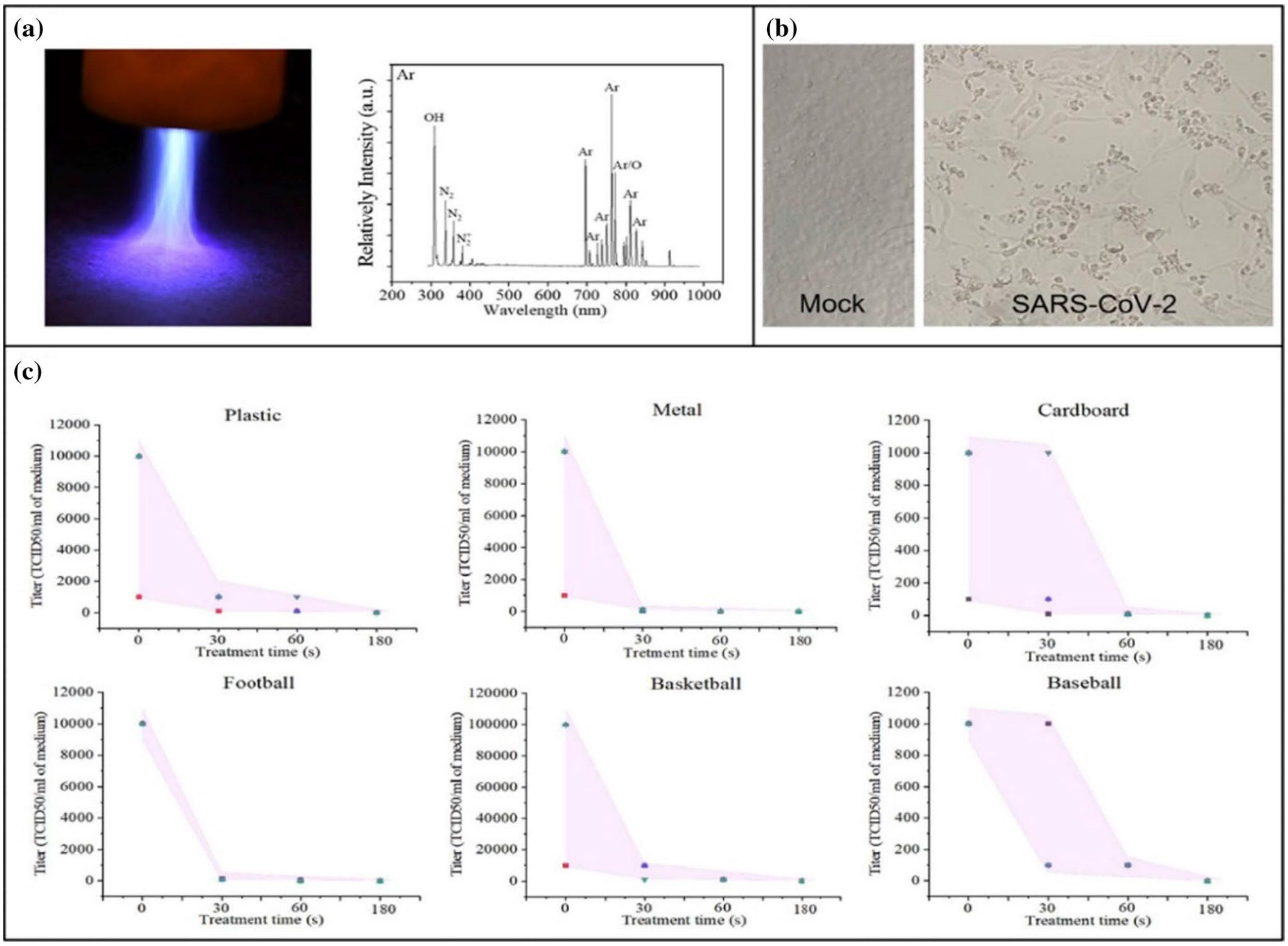

Fig. 35 Argon gas-based plasma discharge disinfecting SARS-CoV-2: **a** Argon plasma treatment of a plastic surface and the optical emission spectra of ROS and RNS (exposure: 250 ms), and **b** the bright-field image of Vero-E6 cells infected with SARS-CoV-2 showing the viral cytopathic effect (CPE). Control of uninfected cells was included in the experiment. **c** Titre response on SARS-CoV-2 to plasma treatment exposures of 0, 30, 60, and 180 s on surfaces of metal, cardboard, plastic, football leather, composite, baseball leather and basketball leather. The distance between the object surface and the plasma device was ~15 mm [35]

or minimal invasiveness, along with ease of use, enhanced wound healing, and inhibition of inflammation [44, 188].

Recently Guo et al. investigated plasma activated water (PAW) as an alternative disinfectant [49]. Disruption of the SARS-COV-2 infection process by damaging the spike protein (S-protein) of the receptor-binding domain (RBD) and by binding to the cellular receptor human angiotensin-converting enzyme 2 (hACE2) was the main target of that study. In the study, pseudoviruses with the S protein of SARS-CoV-2 were used as a model and related mechanisms. The PAW was prepared using a surface discharge plasma device consisting a water-facing grounded mesh electrode and high-voltage plane electrode separated by a polytetrafluoroethylene dielectric layer (Fig. 36). Their aim was to check the antiviral ability of PAW against pseudovirus, thus providing a new disinfection method to fight the pandemic. The PAW damaged or inactivated S-protein incorporated in the pseudovirus of SAR-COV-2 and inhibited the infection process. Species such as $ONOO^-$ and $O_2^{\bullet -}$, (Short-lived species generated in PAW) are assumed to react selectively with proteins. This study will be a nice example for using PAW as a disinfection agent due to its effectiveness, even after long storage (more than 30 days), and strength compared to market available hydrogen peroxide. Thus long-term effectiveness of PAW was shown to provide a basis for the development of a new disinfectant. Further studies on the role of PAW as a disinfectant for SARS-COV-2 and other corona viruses may further support this investigation.

Several investigations have described the effect of cold plasma treatment on various viruses, such as bacteriophages (MS2, Φ174, and T4 strains), human norovirus (NV), feline calicivirus (FCV), porcine reproductive and respiratory syndrome (PPRS), Newcastle disease virus (NDV), murine norovirus (MNV), respiratory syncytial virus (RSV), hepatitis

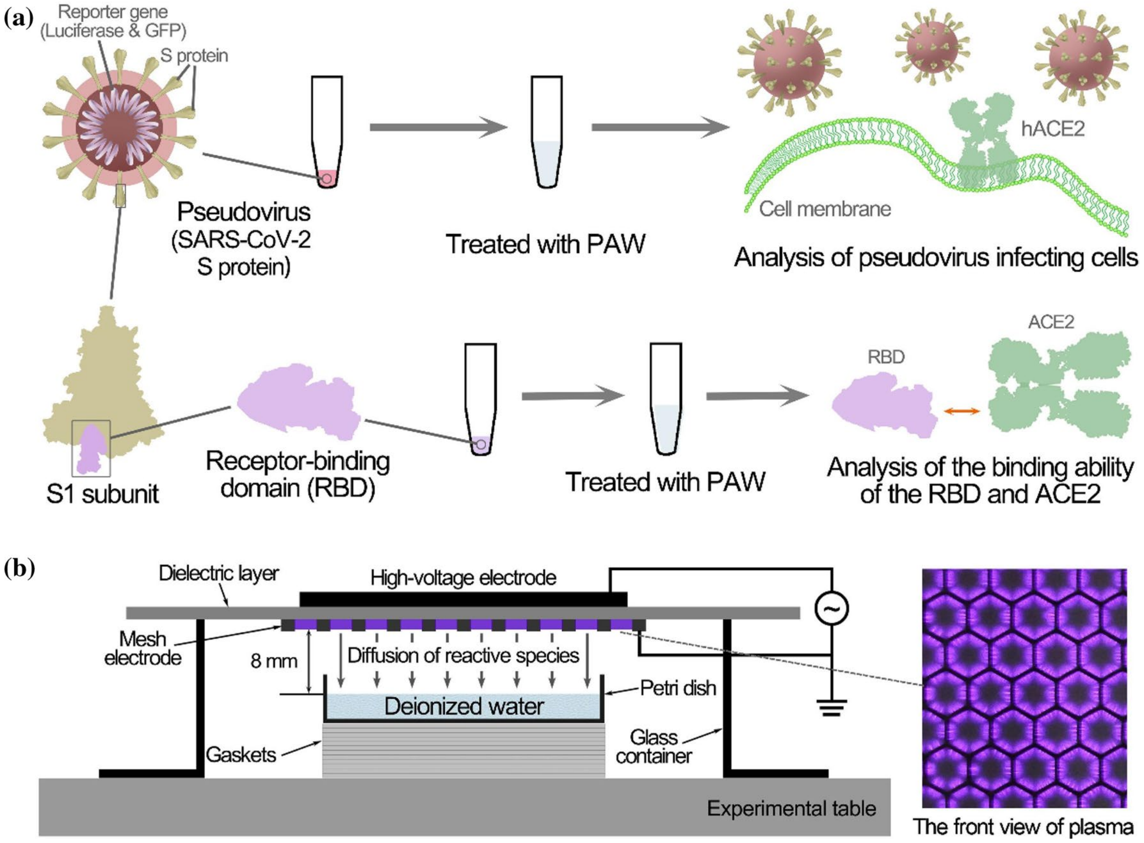

Fig. 36 Plasma-treated water (PAW) as a disinfection agent. **a** Schematic diagram of the pseudovirus study and **b** PAW preparation method using a surface plasma device [49]

A virus (HAV), etc. Plasma-induced ROS and RNS, ozone, as well as some amount of UV, electrons, ions, and other factors can affect structural components such as cell walls or membranes, along with physiological components such as nuclear material and proteins. Nonetheless, definite evidence for the inactivation of virus pathogenesis and a modification of the host–pathogen interaction mechanism by using plasma has been not reported yet. The necessity to study plasma-based virus deactivation mechanisms in both animal models, and cell-based models including organoids against future variants of corona viruses is increasing. The mechanism for the inactivation and control of Coronaviruses will aim at host–pathogen interaction and virulence factor that can provide new perceptiveness for the control of virus pathogenesis by using plasmas.

Human coronaviruses, such as HCoV-229E and HCoV-OC43, HCoV-NL63 and HCoV-HKU1, usually cause mild respiratory tract infections whereas severe acute respiratory syndrome coronavirus (SARS-CoV), Middle East respiratory syndrome coronavirus (MERS-CoV) and SARS-CoV-2, are highly pathogenic. These viruses are present in intermediate hosts such as bats wherein they undergo recombination and mutations forming altered genotypes leading to severe pathogenicity. SARS-CoV-2 enters into human cells by using an interaction between receptor-binding domain (RBD) of SARS-CoV-2 spike (S) protein and the cell surface receptor angiotensin-converting enzyme-2 (ACE2). The viral S-protein further undergoes cleavage by proteases (TMPRS2) or cathepsin B or FURIN to cause fusion of the host cell membrane and an ensuing infection. Recently, studies have shown that the SARS-CoV-2-specific virulence factors are programmed to evade detection and to modulate host immune cells responses, including interferon (IFN) regulation and to utilize the host cell for viral replication. Although several studies have established the role of Spike protein as a virulence factor of SARS-COV-2, the recent variant of SARS-Cov-2 (deletion 69–70, deletion 144, N501Y, A570D, D614G, P681H, T716I, S982A, D1118H) has created open questions as to our understanding of virulence factors. Speculation is that more mutations and variants might emerge from the coronavirus family and might cause future corona virus epidemics or pandemics. A possibility exists that every time we may have to design new vaccines for future corona virus strains. This makes in-depth investigations for plasma-based treatment procedures to control functions of virulence factors or to damage viral genetic material essential.

Plasma-based future research must be based on topics related to use of model viruses (including low pathogenic coronavirus) that can quickly respond to future corona virus threats. To attain this aim, the plasma community must understand the general virological characteristics of coronavirus: invasion into cells during infection, proliferation within cells, release of viruses after proliferation, and transfer to adjacent cells. Finally, we can analyze important factors of pathogenicity after plasma treatment in the coronavirus infection process build advance information, and secure plasma treatment technology for future viruses. For this purpose, we need to focus on virological factors (such as coronavirus infection, replication, life cycle research), immunological factors (such as host immune interactions and immune specificity), pathological factors (research on biological pathogenesis and pathogenicity), and infection characteristics of mutant strains and animal viruses. Using these parameters for analysis after plasma treatment, we can establish a next-generation pandemic infectious disease treatment and sterilization system.

Also, artificial intelligence (AI)-based prediction models can be used to predict possible treatment strategies for the next upcoming mutated virus strains. These AI models can assist in early prediction of virulence properties, which can help to support plasma-based treatments. The development of cost-effective economical plasma-based treatments will provide endless prospects for the treatment of critical stage patients infected with the virus. Furthermore, now is the time to perform investigations and to develop plasma-based devices or products for active treatment of COVID-19 and its variant virus around the world while ensuring safety of the patients and the medical doctors.

Due to environmental safety standards, many researchers are conducting their investigations on inactivation of viruses by using other eco-friendly reactive gases while avoiding high amount of ozone. In addition, the reality is that research on the interaction between a plasma and a virus needs to be recognized as important for clarifying how to inactivate COVID-19 and its variant virus for the development of plasma quarantine devices for human beings. Furthermore, now is the time to conduct research and development while ensuring the safety of patients and medical doctors on the implementation of plasma treatment devices for active treatment of COVID-19 and its variant virus around a world. In addition, the simultaneous development of plasma-treated water needs to be emphasized because the justifications for its use are plentiful.

7 Perspectives and conclusion

Plasma bioscience and medicine are newly developed and rapidly developing, with the goal of next-generation health promotion and disease healing. To this end, the development of nonthermal (or low temperature) atmospheric pressure biocompatible plasma (NBP) source that can be actually applied in the medical field, and research and development of plasma activated water (PAW) using this NBP are actively underway. These NBP and PTW can also be applied to cancer cells, neurodegenerative diseases, and skin diseases, which have difficult treatments. Active cooperative research, such as securing new data and related basic plasma clinical trials are needed. The treatment based on plasma bioscience can be combined with existing cancer treatment methods and can be applied in various ways. For further exploration of recent research has investigated the effect of plasma-treated biomolecules for cancer treatment application [189]. These kind of plasma-treated or activated biomolecules also have the potential for numerous biomedical applications. In particular, the NBP can be expected to have great effects when it can be applied together with plasma treated water to treat liver cancer, lung cancer, brain cancer, breast cancer, pancreatic cancer, skin cancer, and blood cancer, which are known to be types of intractable cancer. Nonthermal plasma-synthesized nanoparticles can also be utilized for cancer treatment and several other biomedical applications. These environmentally friendly synthesized nanoparticles can induce immunogenic cell death and release a damage-associated molecular pattern in cancer cells. Moreover, these nanoparticles exhibit enhanced uptake in malignant cells and less toxicity in normal cells [190]. In addition, the manufacture of, and disinfection of plasma medical devices for surgical trauma treatment, wound healing, burn treatment, and skin disease control and treatment are recognized as very important fields. Moreover, the NBP can be expected to be efficient when sterilizing bacteria resistant to antibiotics. Recent investigations in plasma bioscience and medicine showed the application of a gas plasma for bio-sterilization, decontamination, and water purification [191, 192]. Also, these plasma sources or plasma-activated water with minerals can be used for agriculture applications [193], and this area can be further explored with several new plasma-based sustainable agriculture ideas. Now, in the era of long-lived health and welfare, it is also important to securing cooperative technology to solve this by applying NBP to degenerative brain diseases among the silver generation is important.

In 2015, we need to get a database of realistic wisdom about the valuable experience with the Middle East Respiratory Syndrome (MERS) and the infection of the new virus COVID-19 this year, as seen in the harsh reality. Prevention and inactivation of these viruses in all-weather areas, indoor disinfection of ambulances, indoor air purification and virus removal, water purification and fine dust removal are difficult to implement only with conventional methods. At this time, applying NBP technology can bring better results than expected.

Acknowledgements This study was supported by the National Research Foundation (NRF) of Korea, funded by the Korea government (NRF-2016K1A4A3914113, 2021R1A6A1A03038785).

References

1. F. Massines, G. Gouda, J. Phys. D. Appl. Phys. **31**, 3411–3420 (1998)
2. U. Kogelschatz, Plasma Chem. Plasma Process. **23**, 1–46 (2003)
3. A. Fridman, A. Chirokov, A. Gutsol, J. Phys. D. Appl. Phys. **38**, R1–R24 (2005)
4. J.S. Sousa, G. Bauville, B. Lacour, V. Puech, M. Touzeau, J.-L. Ravanat, Appl. Phys. Lett. **97**, 141502 (2010)
5. M.G. Kong, G. Kroesen, G. Morfill, T. Nosenko, T. Shimizu, J. Van Dijk, J.L. Zimmermann, New J. Phys. **11**, 115012 (2009)
6. J. Winter, K. Wende, K. Masur, S. Iseni, M. Dünnbier, M.U. Hammer, H. Tresp, K.D. Weltmann, S. Reuter, J. Phys. D. Appl. Phys. **46**, 295401 (2013)
7. P. Attri, Y.H. Kim, D.H. Park, J.H. Park, Y.J. Hong, H.S. Uhm, K.-N. Kim, A. Fridman, E.H. Choi, Sci. Rep. **5**, 1–8 (2015)
8. E.H. Choi, H.S. Uhm, N.K. Kaushik, AAPPS Bull. **31**, 1–38 (2021)
9. N. Barekzi, M. Laroussi, IEEE Trans. Plasma Sci. **42**, 2738–2739 (2014)
10. N. Barekzi, M. Laroussi, Plasma Process. Polym. **10**, 1039–1050 (2013)
11. N. Kaushik, N. Uddin, G.B. Sim, Y.J. Hong, K.Y. Baik, C.H. Kim, S.J. Lee, N.K. Kaushik, E.H. Choi, Sci. Rep. **5**, 1–11 (2015)
12. E.H. Choi, Vac. Mag. **7**, 2 (2020)
13. K.N.K. E. H. Choi, Y. H. Kim, Vac. Mag. **38** (2014)
14. E.H. Choi, Vac. Mag. **9** (2015)
15. G.L. Geison, Isis **60**, 273–292 (1969)
16. S.L. Miller et al., Science **117**, 528–529 (1953)
17. J.D. Watson, F.H.C. Crick, Nature **171**, 737–738 (1953)
18. T. von Woedtke, A. Schmidt, S. Bekeschus, K. Wende, K.-D. Weltmann, In Vivo (Brooklyn) **33**, 1011–1026 (2019)
19. M. Laroussi, Front. Phys. **8**, 74 (2020)
20. J.-Y. Jang, Y.J. Hong, J. Lim, J.S. Choi, E.H. Choi, S. Kang, H. Rhim, Biomaterials **156**, 258–273 (2018)
21. X. Lu, M. Keidar, M. Laroussi, E. Choi, E.J. Szili, K. Ostrikov, Mater. Sci. Eng. R Rep. **138**, 36–59 (2019)
22. D. Dobrynin, G. Fridman, G. Friedman, A. Fridman, New J. Phys. **11**, 115020 (2009)
23. M. Ito, J.-S. Oh, T. Ohta, M. Shiratani, M. Hori, Plasma Process. Polym. **15**, 1700073 (2018)
24. J.-S. Song, S.B. Kim, S. Ryu, J. Oh, D.-S. Kim, Front. Plant Sci. **11**, 988 (2020)
25. C. Smet, M. Baka, A. Dickenson, J.L. Walsh, V.P. Valdramidis, J.F. Van Impe, Plasma Process. Polym. **15**, 1700048 (2018)
26. B. Adhikari, M. Adhikari, B. Ghimire, G. Park, E.H. Choi, Sci. Rep. **9**, 1–15 (2019)
27. P. Attri, K. Ishikawa, T. Okumura, K. Koga, M. Shiratani, Processes **8**, 1002 (2020)
28. B. Adhikari, K. Pangomm, M. Veerana, S. Mitra, G. Park, Front. Plant Sci. **11**, 77 (2020)
29. P.J. Cullen, J. Lalor, L. Scally, D. Boehm, V. Milosavljević, P. Bourke, K. Keener, Plasma Process. Polym. **15**, 1700085 (2018)
30. G. Pauzaite, A. Malakauskiene, Z. Nauciene, R. Zukiene, I. Filatova, V. Lyushkevich, I. Azarko, V. Mildaziene, Plasma Process. Polym. **15**, 1700068 (2018)
31. V. Mildaziene, G. Pauzaite, Z. Naucienė, A. Malakauskiene, R. Zukiene, I. Januskaitiene, V. Jakstas, L. Ivanauskas, I. Filatova, V. Lyushkevich, Plasma Process. Polym. **15**, 1700059 (2018)
32. C. Szőke, Z. Nagy, K. Gierczik, A. Székely, T. Spitkól, Z.T. Zsuboril, G. Galiba, C.L. Marton, K. Kutasi, Plasma Process. Polym. **15**, 1700138 (2018)
33. Y. Park, K.S. Oh, J. Oh, D.C. Seok, S.B. Kim, S.J. Yoo, M.-J. Lee, Plasma Process. Polym. **15**, 1600056 (2018)
34. V. Štěpánová, P. Slavíček, J. Kelar, J. Prášil, M. Smékal, M. Stupavská, J. Jurmanová, M. Černák, Plasma Process. Polym. **15**, 1700076 (2018)
35. J.-S. Kwon, S.-H. Choi, E.H. Choi, K.-M. Kim, P.K. Chu, Int. J. Mol. Sci. **21**, 6085 (2020)
36. M.-J. Lee, J.-S. Kwon, H.B. Jiang, E.H. Choi, G. Park, K.-M. Kim, Sci. Rep. **9**, 1–13 (2019)
37. S.-H. Seo, I. Han, H.S. Lee, J.J. Choi, E.H. Choi, K.-N. Kim, G. Park, K.-M. Kim, Sci. Rep. **7**, 1–11 (2017)
38. T.T. Gupta, S.B. Karki, J.S. Matson, D.J. Gehling, H. Ayan, Biomed Res. Int. **2017**, 6085741 (2017)
39. H. Wu, C. Moser, H.-Z. Wang, N. Høiby, Z.-J. Song, Int. J. Oral Sci. **7**, 1–7 (2015)
40. B. Gomes, S.F.C. Souza, C.C.R. Ferraz, F.B. Teixeira, A.A. Zaia, L. Valdrighi, F.J. Souza-Filho et al., Int. Endod. J. **36**, 267–275 (2003)
41. S.R. Herbst, M. Hertel, H. Ballout, P. Pierdzioch, K.-D. Weltmann, H.C. Wirtz, S. Abu-Sirhan, E. Kostka, S. Paris, S. Preissner, Open Dent. J. **9**, 486 (2015)
42. R.O. Darouiche, N. Engl, J. Med. **350**, 1422–1429 (2004)
43. L. Hall-Stoodley, J.W. Costerton, P. Stoodley, Nat. Rev. Microbiol. **2**, 95–108 (2004)
44. A. Filipić, I. Gutierrez-Aguirre, G. Primc, M. Mozetič, D. Dobnik, Trends Biotechnol. **38**(11), 1278–1291 (2020)
45. J.H. Park, N. Kumar, D.H. Park, M. Yusupov, E.C. Neyts, C.C.W. Verlackt, A. Bogaerts, M.H. Kang, H.S. Uhm, E.H. Choi et al., Sci. Rep. **5**, 1–14 (2015)
46. R. Kar, N. Chand, A. Bute, N. Maiti, A.N. Rao, V. Nagar, R. Shashidhar, D.S. Patil, S.K. Ghosh, A. Sharma, Trans. Indian Natl. Acad. Eng. **5**, 327–331 (2020)
47. A. Bisag, P. Isabelli, R. Laurita, C. Bucci, F. Capelli, G. Dirani, M. Gherardi, G. Laghi, A. Paglianti, V. Sambri, V. Colombo, Plasma Process. Polym. **17**, 2000154 (2020)
48. T. Xia, A. Kleinheksel, E.M. Lee, Z. Qiao, K.R. Wigginton, H.L. Clack, J. Phys. D. Appl. Phys. **52**, 255201 (2019)
49. L. Guo, Z. Yao, L. Yang, H. Zhang, Y. Qi, L. Gou, W. Xi, D. Liu, L. Zhang, Y. Cheng, X. Wang, M. Rong, H. Chen, M.G. Kong, Chem. Eng. J. **421**, 127742 (2020)
50. T. Bernhardt, M.L. Semmler, M. Schäfer, S. Bekeschus, S. Emmert, L. Boeckmann, Oxid. Med. Cell. Longev. **2019**, 1–10 (2019)
51. T. von Woedtke, S. Emmert, H.-R. Metelmann, S. Rupf, K.-D. Weltmann, Phys. Plasmas **27**, 70601 (2020)
52. N.K. Kaushik, N. Kaushik, R. Wahab, P. Bhartiya, N.N. Linh, F. Khan, A.A. Al-Khedhairy, E.H. Choi, Cancers (Basel) **12**, 457 (2020)
53. A.A. Fridman, G.G. Friedman, *Plasma medicine* (Wiley, Chichester, 2013)
54. M. Laroussi, M.G. Kong, G. Morfill, W. Stolz, *Plasma medicine: applications of low-temperature gas plasmas in medicine and biology* (Cambridge University Press, Cambridge, 2012)

55. A. Bogaerts, M. Yusupov, J. der Paal, C.C.W. Verlackt, E.C. Neyts, Plasma Process. Polym. **11**, 1156–1168 (2014)
56. H. Tanaka, M. Hori, J. Clin. Biochem. Nutr. **60**, 16–67 (2017)
57. H.-R. Metelmann, T. Von Woedtke, K.-D. Weltmann, *Comprehensive clinical plasma medicine: cold physical plasma for medical application* (Springer, 2018)
58. S. Toyokuni, Y. Ikehara, F. Kikkawa, M. Hori, *Plasma medical science* (Academic Press, 2018)
59. X. Lu, G.V. Naidis, M. Laroussi, S. Reuter, D.B. Graves, K. Ostrikov, Phys. Rep. **630**, 1–84 (2016)
60. E.J. Szili, J.-S. Oh, H. Fukuhara, R. Bhatia, N. Gaur, C.K. Nguyen, S.-H. Hong, S. Ito, K. Ogawa, C. Kawada, Plasma Sourc. Sci. Technol. **27**, 14001 (2017)
61. D. Liu, E.J. Szili, K. Ken-Ostrikov, Plasma Process. Polym. **17**, 2000097 (2020)
62. E. Turrini, A. Stancampiano, E. Simoncelli, R. Laurita, E. Catanzaro, C. Calcabrini, M. Gherardi, V. Colombo, C. Fimognari, Clin. Plasma Med. **9**, 15–16 (2018)
63. N. Kaushik, S.J. Lee, T.G. Choi, K.Y. Baik, H.S. Uhm, C.H. Kim, N.K. Kaushik, E.H. Choi, Sci. Rep. **5**, 1–11 (2015)
64. I. Adamovich, S.D. Baalrud, A. Bogaerts, P.J. Bruggeman, M. Cappelli, V. Colombo, U. Czarnetzki, U. Ebert, J.G. Eden, P. Favia et al., J. Phys. D. Appl. Phys. **50**, 323001 (2017)
65. D. Yan, Q. Wang, M. Adhikari, A. Malyavko, L. Lin, D.B. Zolotukhin, X. Yao, M. Kirschner, J.H. Sherman, M. Keidar, ACS Appl. Mater. Interfaces **12**, 34548–34563 (2020)
66. N.K. Kaushik, N. Kaushik, K.C. Yoo, N. Uddin, J.S. Kim, S.J. Lee, E.H. Choi, Biomaterials **87**, 118–130 (2016)
67. D. Trachootham, J. Alexandre, P. Huang, Nat. Rev. Drug Discov. **8**, 579–591 (2009)
68. J. Šimečková, F. Krčma, D. Klofáč, L. Dostál, Z. Kozáková, Water **12**, 2357 (2020)
69. S. Jung, H.J. Kim, S. Park, H.I. Yong, J.H. Choe, H.-J. Jeon, W. Choe, C. Jo, Meat Sci. **108**, 132–137 (2015)
70. P. Shaw, N. Kumar, H.S. Kwak, J.H. Park, H.S. Uhm, A. Bogaerts, E.H. Choi, P. Attri, Sci. Rep. **8**, 11268 (2018)
71. U. Schnabel, O. Handorf, K. Yarova, B. Zessin, S. Zechlin, D. Sydow, E. Zellmer, J. Stachowiak, M. Andrasch, H. Below, Foods **8**, 55 (2019)
72. A. Azzariti, R.M. Iacobazzi, R. Di Fonte, L. Porcelli, R. Gristina, P. Favia, F. Fracassi, I. Trizio, N. Silvestris, G. Guida et al., Sci. Rep. **9**, 1–13 (2019)
73. P. Attri, J.H. Park, A. Ali, E.H. Choi, Anti-Cancer Agents Med. Chem. **18**, 805–814 (2018)
74. N. Yoshikawa, W. Liu, K. Nakamura, K. Yoshida, Y. Ikeda, H. Tanaka, M. Mizuno, S. Toyokuni, M. Hori, F. Kikkawa et al., Sci. Rep. **10**, 1–8 (2020)
75. H.S. Uhm, E.H. Choi, G. Cho, Phys. Plasmas **7**, 2744–2746 (2000)
76. H.S. Uhm, E.H. Choi, G.S. Cho, Appl. Phys. Lett. **78**, 592–594 (2001)
77. M. Keidar, *Plasma cancer therapy* (Springer, 2020)
78. Evaluation guideline for plasma wound treatment (Ministry of Food and Drug and Safety, Korean Government, 2016.12)” (2016)
79. 21CFR801, “21CFR801.415 Maximum acceptable level of ozone":"KS C9314 Standards of interior air cleaner (SPS-KACA 002-0132)":"Criterion for chemical substance and physical factor exposure" from Ministry of Employment and Labor Notice #2020-48, Korea” (2020)
80. H.S. Uhm, E.H. Choi, G. Cho, K.W. Whang, Jpn. J. Appl. Phys. **40**, L295 (2001)
81. G. Cho, Y.-G. Kim, Y.-S. Kim, D.-G. Joh, E.-H. Choi, Jpn. J. Appl. Phys. **37**, L1178 (1998)
82. H.D. Hagstrum, Phys. Rev. **96**, 336 (1954)
83. J.Y. Lim, J.S. Oh, B.D. Ko, J. Won-Cho, S.O. Kang, G. Cho, H.S. Uhm, E.H. Choi, J. Appl. Phys. **94**, 764–769 (2003)
84. B. Ghimire, E.J. Szili, P. Lamichhane, R.D. Short, J.S. Lim, P. Attri, K. Masur, K.-D. Weltmann, S.-H. Hong, E.H. Choi, Appl. Phys. Lett. **114**, 93701 (2019)
85. N. Srivastava, C. Wang, J. Appl. Phys. **110**, 53304 (2011)
86. Y.J. Hong, C.J. Nam, K.B. Song, G.S. Cho, H.S. Uhm, D.I. Choi, E.H. Choi, J. Instrum. **7**, C03046 (2012)
87. B. Ghimire, J. Sornsakdanuphap, Y.J. Hong, H.S. Uhm, K.D. Weltmann, E.H. Choi, Phys. Plasmas **24**, 073502 (2017)
88. C. Bogdan, Nat. Immunol. **2**, 907–916 (2001)
89. H.-P. Dorn, R. Neuroth, A. Hofzumahaus, J. Geophys. Res. Atmos. **100**, 7397–7409 (1995)
90. Y.H. Kim, Y.J. Hong, K.Y. Baik, G.C. Kwon, J.J. Choi, G.S. Cho, H.S. Uhm, E.H. Choi et al., Plasma Chem. Plasma Process. **34**, 457–472 (2014)
91. T.E.L. Smith, M.J. Wooster, M. Tattaris, D.W.T. Griffith, Atmos Meas. Tech. **4**, 97–116 (2011)
92. S. Kassi, K. Didriche, C. Lauzin, X. De Ghellinck D’Elseghem Vaernewijckb, A. Rizopoulos, M. Herman, Spectrochim Acta Part A Mol Biomol Spectrosc **75**, 142–145 (2010)
93. Z. Du, S. Zhang, J. Li, N. Gao, K. Tong, Appl. Sci. **9**, 338 (2019)
94. S. Iséni, S. Reuter, K.-D. Weltmann, J. Phys. D. Appl. Phys. **47**, 75203 (2014)
95. J.P. Burrows, A. Dehn, B. Deters, S. Himmelmann, A. Richter, S. Voigt, J. Orphal, J. Quant. Spectrosc. Radiat. Transf. **60**, 1025–1031 (1998)
96. Y.J. Hong, J. Lim, J.S. Choi, K.D. Weltmann, E.H. Choi, Plasma Process. Polym. **18**, 2000168 (2021)
97. X.-M. Zhu, Y.-K. Pu, J. Phys. D. Appl. Phys. **43**, 403001 (2010)
98. X.-M. Zhu, Y.-K. Pu, Phys. Plasmas **12**, 103501 (2005)
99. L.G. Piper, J. Chem. Phys. **97**, 270–275 (1992)
100. V. Guerra, J. Loureiro, Plasma Sources Sci. Technol. **6**, 361 (1997)
101. A. Lofthus, P.H. Krupenie, J. Phys. Chem. Ref. Data **6**, 113–307 (1977)
102. S. Nunomura, M. Kondo, H. Akatsuka, Plasma Sources Sci. Technol. **15**, 783 (2006)
103. Y. Fuxiang, M. Zongxin, Z. Jialiang, Plasma Sci. Technol. **18**, 79 (2016)
104. B. Ghimire, P. Lamichhane, J.S. Lim, B. Min, R. Paneru, K.-D. Weltmann, E.H. Choi, Appl. Phys. Lett. **113**, 194101 (2018)
105. B. Ghimire, E.J. Szili, P. Lamichhane, R.D. Short, J.S. Lim, P. Attri, K. Masur, K.D. Weltmann, S.H. Hong, E.H. Choi, Appl. Phys. Lett. **114**, 093701 (2019)
106. P. Svarnas, Plasma Sci. Technol. **15**, 891 (2013)
107. W. Tian, M.J. Kushner, J. Phys. D. Appl. Phys. **48**, 494002 (2015)
108. A. Starikovskiy, Y. Yang, Y.I. Cho, A. Fridman, Plasma Sources Sci. Technol. **20**, 24003 (2011)
109. S. Kanazawa, H. Kawano, S. Watanabe, T. Furuki, S. Akamine, R. Ichiki, T. Ohkubo, M. Kocik, J. Mizeraczyk, Plasma Sources Sci. Technol. **20**, 34010 (2011)
110. P. Attri, Y.H. Kim, D.H. Park, J.H. Park, Y.J. Hong, H.S. Uhm, K.-N. Kim, A. Fridman, E.H. Choi, Sci. Rep. **5**, 9332 (2015)
111. J.S. Lim, R.H. Kim, Y.J. Hong, P. Lamichhane, B.C. Adhikari, J. Choi, E.H. Choi, Results Phys. **19**, 103569 (2020)
112. J.S. Lim, Y.J. Hong, B. Ghimire, J. Choi, S. Mumtaz, E.H. Choi, Results Phys. **20**, 103693 (2021)
113. N.C. Roy, M.G. Hafez, M.R. Talukder, Phys. Plasmas **23**, 83502 (2016)
114. P. Bruggeman, D.C. Schram, Plasma Sources Sci. Technol. **19**, 045025 (2010)
115. D.-X. Liu, P. Bruggeman, F. Iza, M.-Z. Rong, M.G. Kong, Plasma Sources Sci. Technol. **19**, 25018 (2010)
116. Y. Itikawa, N. Mason, J. Phys. Chem. Ref. Data (2005). https://doi.org/10.1063/1.1799251

117. IEC 60601-1-1. Medical electrical equipment—part 1–1: general requirements for safety—colateral standard: safety requirements for medical electrical systems
118. N. Leitgeb, *Sicherheit von Medizingeräten: Recht-Risiko-Chancen* (Springer-Verlag, 2015)
119. M.S. Mann, R. Tiede, K. Gavenis, G. Daeschlein, R. Bussiahn, K.-D. Weltmann, S. Emmert, T. von Woedtke, R. Ahmed, Clin. Plasma Med. **4**, 35–45 (2016)
120. A. Moldgy, G. Nayak, H.A. Aboubakr, S.M. Goyal, P.J. Bruggeman, J. Phys. D. Appl. Phys. **53**, 434004 (2020)
121. M.J. Nicol, T.R. Brubaker, B.J. Honish, A.N. Simmons, A. Kazemi, M.A. Geissel, C.T. Whalen, C.A. Siedlecki, S.G. Bilén, S.D. Knecht et al., Sci. Rep. **10**, 1–11 (2020)
122. E.C. Filippidou, A. Koukouliata, Arch. Hell. Med. Ellenikes Iatrikes, **28**, (2011)
123. J. Gamble, W. Jones, S. Minshall, Environ. Res. **44**, 6–17 (1987)
124. W.F. McDonnell, D.E. Abbey, N. Nishino, M.D. Lebowitz, Environ. Res. **80**, 110–121 (1999)
125. J. Luo, A.F. Chen, Acta Pharmacol. Sin. **26**, 259–264 (2005)
126. Y. Yang, P.K. Qi, Z.L. Yang, N. Huang, Biosurf. Biotribol. **1**, 177–201 (2015)
127. P. Boukamp, R.T. Petrussevska, D. Breitkreutz, J. Hornung, A. Markham, N.E. Fusenig, J. Cell Biol. **106**, 761–771 (1988)
128. R. Bussiahn, N. Lembke, R. Gesche, T. von Woedtke, K.D. Weltmann, Hyg. Med **38**, 212–216 (2013)
129. B.R.W.K.-D.R.M.K.R.P.F. Metelmann H-R von Woedtke Th, W.P. D, Am. J. Cosmet. Surg., **29**, 52 (2012)
130. P. Attri, K. Koga, M. Shiratani, Appl. Phys. Express **14**, 27002 (2021)
131. M.-S. Choi, E.B. Jeon, J.Y. Kim, E.H. Choi, J.S. Lim, J. Choi, S.Y. Park, J. Food Eng. **278**, 109952 (2020)
132. M. Adhikari, N. Kaushik, B. Ghimire, B. Adhikari, S. Baboota, A.A. Al-Khedhairy, R. Wahab, S.-J. Lee, N.K. Kaushik, E.H. Choi, Cell Commun Signal. **17**, 1–14 (2019)
133. A. Nasir, G. Caetano-Anollés, Sci. Adv. **1**, e1500527 (2015)
134. G. Bauer, Plasma Med. **9**, 1 (2019)
135. G. Bauer, Redox Biol. **26**, 101291 (2019)
136. G. Bauer, D. Sersenová, D.B. Graves, Z. Machala, Sci. Rep. **9**, 1–28 (2019)
137. A. Dubuc, P. Monsarrat, F. Virard, N. Merbahi, J.P. Sarrette, S. Laurencin-Dalicieux, S. Cousty, Therap Adv Med Oncol **10**, 1–12 (2018)
138. X. Zhou, D. Cai, S. Xiao, M. Ning, R. Zhou, S. Zhang, X. Chen, K. Ostrikov, X. Dai, J. Cancer **11**, 2273 (2020)
139. F. Saadati, H. Mahdikia, H.-A. Abbaszadeh, M.-A. Abdollahifar, M.S. Khoramgah, B. Shokri, Sci. Rep. **8**, 1–15 (2018)
140. L. Xiang, X. Xu, S. Zhang, D. Cai, X. Dai, Free Radic. Biol. Med. **124**, 205–213 (2018)
141. X. Cheng, W. Rowe, L. Ly, A. Shashurin, T. Zhuang, S. Wigh, G. Basadonna, B. Trink, M. Keidar, J. Canady, Plasma **1**, 218–228 (2018)
142. M. Keidar, D. Yan, I.I. Beilis, B. Trink, J.H. Sherman, Trends Biotechnol. **36**, 586–593 (2018)
143. K.J. Schlegel, B. Veronika, Clin. Plasma Med. **1**, 2 (2013)
144. D. Yan, H. Cui, W. Zhu, N. Nourmohammadi, J. Milberg, L.G. Zhang, J.H. Sherman, M. Keidar, Sci. Rep. **7**, 1–12 (2017)
145. G.I. Deichman, Biochemistry **65**, 78–94 (2000)
146. B. Böhm, S. Heinzelmann, M. Motz, G. Bauer, Biol. Chem. **396**, 1339–1356 (2015)
147. G. Bauer, D.B. Graves, Plasma Process. Polym. **13**, 1157–1178 (2016)
148. H. Mokhtari, L. Farahmand, K. Yaserian, N. Jalili, K. Majidzadeh-A, J. Cell. Physiol. **234**, 6778–6782 (2019)
149. A. Lin, Y. Gorbanev, J. De Backer, J. Van Loenhout, W. Van Boxem, F. Lemière, P. Cos, S. Dewilde, E. Smits, A. Bogaerts, Adv. Sci. **6**, 1802062 (2019)
150. A. Lin, B. Truong, S. Patel, N. Kaushik, E.H. Choi, G. Fridman, A. Fridman, V. Miller, Int. J. Mol. Sci. **18**, 966 (2017)
151. A.G. Lin, B. Xiang, D.J. Merlino, T.R. Baybutt, J. Sahu, A. Fridman, A.E. Snook, V. Miller, Oncoimmunology **7**, e1484978 (2018)
152. S. Bekeschus, J. Kolata, C. Winterbourn, A. Kramer, R. Turner, K.D. Weltmann, B. Bröker, K. Masur, Free Radic. Res. **48**, 542–549 (2014)
153. H.J. Ahn, K. Il-Kim, N.N. Hoan, C.H. Kim, E. Moon, K.S. Choi, S.S. Yang, J.-S. Lee, PLoS ONE **9**, e86173 (2014)
154. N.K. Kaushik, N. Kaushik, B. Min, K.H. Choi, Y.J. Hong, V. Miller, A. Fridman, E.H. Choi, J. Phys. D. Appl. Phys. **49**, 84001 (2016)
155. N.K. Kaushik, N. Kaushik, M. Adhikari, B. Ghimire, N.N. Linh, Y.K. Mishra, S.-J. Lee, E.H. Choi, Cancers (Basel) **11**, 842 (2019)
156. F. Virard, S. Cousty, J.-P. Cambus, A. Valentin, P. Kémoun, F. Clément, PLoS ONE **10**, e0133120 (2015)
157. C. Schneider, L. Gebhardt, S. Arndt, S. Karrer, J.L. Zimmermann, M.J.M. Fischer, A.-K. Bosserhoff, Sci. Rep. **8**, 1–10 (2018)
158. K. Wende, S. Straßenburg, B. Haertel, M. Harms, S. Holtz, A. Barton, K. Masur, T. von Woedtke, U. Lindequist, Cell Biol. Int. **38**, 412–425 (2014)
159. A.M. Hirst, M.S. Simms, V.M. Mann, N.J. Maitland, D. O'connell, F.M. Frame, Br. J. Cancer **112**, 1536–1545 (2015)
160. J. Köritzer, V. Boxhammer, A. Schäfer, T. Shimizu, T.G. Klämpfl, Y.-F. Li, C. Welz, S. Schwenk-Zieger, G.E. Morfill, J.L. Zimmermann, PLoS ONE **8**, e64498 (2013)
161. S. Lee, H. Lee, D. Jeong, J. Ham, S. Park, E.H. Choi, S.J. Kim, Free Radic. Biol. Med. **110**, 280–290 (2017)
162. I. Eke, N. Cordes, Semin. Cancer Biol. **31**, 65–75 (2015)
163. N.K. Kaushik, N. Kaushik, N.N. Linh, B. Ghimire, A. Pengkit, J. Sornsakdanuphap, S.J. Lee, E.H. Choi, Nanomaterials **9**, 1–19 (2019)
164. L.N. Nguyen, N. Kaushik, P. Lamichhane, S. Mumtaz, R. Paneru, P. Bhartiya, J.S. Kwon, Y.K. Mishra, L.Q. Nguyen, N.K. Kaushik et al., Green Chem. **22**, 6588–6599 (2020)
165. X. Dai, K. Bazaka, D.J. Richard, E.R.W. Thompson, K.K. Ostrikov, Trends Biotechnol. **36**, 1183–1198 (2018)
166. E. Biscop, A. Lin, W. Van Boxem, J. Van Loenhout, J. De Backer, C. Deben, S. Dewilde, E. Smits, A. Bogaerts, Cancers (Basel) **11**, 1287 (2019)
167. W. Van Boxem, J. der Paal, Y. Gorbanev, S. Vanuytsel, E. Smits, S. Dewilde, A. Bogaerts, Sci. Rep. **7**, 1–15 (2017)
168. P.-M. Girard, A. Arbabian, M. Fleury, G. Bauville, V. Puech, M. Dutreix, J.S. Sousa, Sci. Rep. **6**, 1–17 (2016)
169. N. Kurake, H. Tanaka, K. Ishikawa, T. Kondo, M. Sekine, K. Nakamura, H. Kajiyama, F. Kikkawa, M. Mizuno, M. Hori, Arch. Biochem. Biophys. **605**, 102–108 (2016)
170. E. Griseti, N. Merbahi, M. Golzio, Cancers (Basel) **12**, 721 (2020)
171. K.R. Liedtke, S. Bekeschus, A. Kaeding, C. Hackbarth, J.-P. Kuehn, C.-D. Heidecke, W. von Bernstorff, T. von Woedtke, L.I. Partecke, Sci. Rep. **7**, 1–12 (2017)
172. G. Isbary, J. Köritzer, A. Mitra, Y.-F. Li, T. Shimizu, J. Schroeder, J. Schlegel, G.E. Morfill, W. Stolz, J.L. Zimmermann, Clin. Plasma Med. **1**, 36–44 (2013)
173. J. Gay-Mimbrera, M.C. Garcia, B. Isla-Tejera, A. Rodero-Serrano, A.V. Garcia-Nieto, J. Ruano, Adv. Ther. **33**, 894–909 (2016)
174. Z. Xiong, Trends Biotechnol. **36**, 582–583 (2018)
175. M. Akter, A. Jangra, S.A. Choi, E.H. Choi, I. Han, Cancers (Basel) **12**, 245 (2020)
176. M. Akter, J.S. Lim, E.H. Choi, I. Han, Cells **10**, 236 (2021)

177. Y. Li, M.H. Kang, H.S. Uhm, G.J. Lee, E.H. Choi, I. Han, Sci. Rep. **7**, 1–9 (2017)
178. C.-H. Song, P. Attri, S.-K. Ku, I. Han, A. Bogaerts, E.H. Choi, J. Phys. D. Appl. Phys. **54**, 185202 (2021)
179. Y. Li, J.H. Kim, E.H. Choi, I. Han, Sci. Rep. **9**, 1–10 (2019)
180. I. Han, E.H. Choi, Oncotarget **8**, 36399 (2017)
181. Y. Li, E.H. Choi, I. Han, Oxid. Med. Cell. Longev. **2019**, 2318680 (2019)
182. S.W. Wilhelm, C.A. Suttle, Bioscience **49**, 781–788 (1999)
183. F.G. Dobrynin, D. Fridman, F.A. Fridman, New J. Phys. **11**, 115020 (2009)
184. C. Tendero, C. Tixier, P. Tristant, J. Desmaison, P. Leprince, Spectrochim. Acta Part B At. Spectrosc. **61**(2), 30 (2006)
185. M. Laroussi, IEEE Trans. Plasma Sci. **24**, 1188–1191 (1996)
186. S. Bekeschus, A. Kramer, E. Suffredini, T. Von Woedtke, V. Colombo, IEEE Trans. Radiat. Plasma Med. Sci. **4**, 391–399 (2020)
187. Z. Chen, G. Garcia Jr., V. Arumugaswami, R.E. Wirz, Phys. Fluids **32**, 111702 (2020)
188. M. Weiss, G. Daeschlein, A. Kramer, M. Burchardt, S. Brucker, D. Wallwiener, M.B. Stope, J. Med. Virol. **89**, 952–959 (2017)
189. L.N. Nguyen, N. Kaushik, P. Bhartiya, S.K. Gurmessa, H.-J. Kim, L.Q. Nguye, N.K. Kaushik, E.H. Choi, J. Ind. Eng. Chem. (2021). https://doi.org/10.1016/j.jiec.2021.05.035
190. P. Attri, N.K. Kaushik, N. Kaushik, D. Hammerschmid, A. Privat-Maldonado, J. De Backer, M. Shiratani, E.H. Choi, A. Bogaerts, Int. J. Biol. Macromol. **182**, 1724 (2021)
191. A. Barjasteh, Z. Dehghani, P. Lamichhane, N. Kaushik, E.H. Choi, N.K. Kaushik, Appl. Sci. **11**, 3372 (2021)
192. N.K. Kaushik, S. Bekeschus, H. Tanaka, A. Lin, E.H. Choi, Appl. Sci. **11**, 4584 (2021)
193. P. Lamichhane, M. Veerana, J.S. Lim, S. Mumtaz, B. Shrestha, N.K. Kaushik, G. Park, E.H. Choi, Int. J. Mol. Sci. **22**, 5360 (2021)